Measurement Of The Front Back Asymmetry In Top-Antitop Quark Pairs Produced In $p\bar{p}$ Collisions At $\sqrt{s} = 1.96$ TeV

by

Thomas A Schwarz

A dissertation submitted in partial fulfillment
of the requirements for the degree of
Doctor of Philosophy
(Physics)
in The University of Michigan
2006

Doctoral Committee:

Professor Dante E. Amidei, Chair
Professor James W. Allen
Professor John K. Riles
Professor Kamal Sarabandi
Associate Professor James D. Wells

DEDICATION

To Sara and Mira

ACKNOWLEDGEMENTS

The work presented in this thesis would not have been possible without the help and support from several colleagues, friends, and family members.

I would first and foremost like to acknowledge my wife Sara. She has provided constant support throughout this entire process. I have no doubt that I could not have been able to complete this work without her. She serves as my motivation and my grounding. I have no better friend, and I cannot possibly thank her enough for this. I would also like to thank my daughter Mira, who provides me with constant joy and satisfaction in life. Having her as a daughter means everything to me and spending time with her each day keeps my life in perspective.

My parents, Tom and JoAnn Schwarz, deserve special thanks for their continued love and support. I cannot put into words how much their loyalty means to me. Throughout my life, they have been my strongest advocates and credit for any of my accomplishments must always partially lie with them. My sisters, Jessica, Katie and Megan, are always a source of love, support, and humor. Also my in-laws, Bob, Lance, Paul, and Susan Soderstrom, have always provided support, love, and sometimes entertainment.

I'd like to thank my friends in the Michigan physics department; especially Matt Brown, Ben Burrington, Josh Davis, and Ben Koester with whom I've had many interesting conversations on topics ranging from football to field theory.

I am indebted to my adviser and friend Dan Amidei. He has given me the guidance to

learn my craft and the freedom to explore my creativity. I believe I could not have had a better mentor, and I look forward to our continued collaboration and friendship.

I would like to thank the rest of current and former members of the Michigan CDF Group for their support and guidance: Ken Bloom, Myron Campbell, Kathy Copic, Clark Cully, Dave Gerdes, Nate Goldschmidt, Bo Jayatilaka, Michael Kagan, Stephen Miller, Mitch Soderberg, Monica Tecchio, Tom Wright, and Alexei Varganov.

This thesis would not have been possible without the dedicated efforts of the hundreds of members of the CDF collaboration. I appreciate their dedication and effort in this noble enterprise. I would like to especially acknowledge John Conway, Robin Erbacher, Rob Roser, and Evelyn Thomson, who have provided me with constant support and advice.

Finally, I would like to thank my committee members Prof. Allen, Prof. Riles, Prof. Sarabandi, and Prof. Wells for their time and guidance in this process.

TABLE OF CONTENTS

LIST OF FIGURES

Figure

LIST OF TABLES

Table

CHAPTER 1

Introduction

Quarks, along with leptons and force carrying particles, are predicted by the Standard Model to be the fundamental constituents of nature. In distinction from the leptons, the quarks interact strongly through the chromodynamic force and are bound together within the hadrons. The familiar proton and neutron are bound states of the light "up" and "down" quarks. The most massive quark by far, the "top" quark, was discovered by the CDF and D0 experiments in March, 1995. The new quark was observed in $p\bar{p}$ collisions at 1.8 TeV at the Fermilab Tevatron [1]. The mass of the top quark was measured to be 176 ± 13 GeV/c^2 and the cross section $6.8^{+3.6}_{-2.4}$ pb. It is the $Q = 2/3$, $T_3 = +1/2$ member of the third generation weak-isospin doublet along with the bottom quark. The top quark is the final Standard Model quark to be discovered. Along with whatever is responsible for electroweak symmetry breaking, top quark physics is considered one of the least understood sectors of the Standard Model and represents a front line of our understanding of particle physics.

Currently, the only direct measurements of top quark properties come from the CDF and D0 experiments observing $p\bar{p}$ collisions at the Tevatron. Top quark production at the Tevatron is almost exclusively by quark-antiquark annihilation, $q\bar{q} \rightarrow t\bar{t}$ (85%), and gluon fusion, $gg \rightarrow t\bar{t}$ (15%), mediated by the strong force [2]. The theoretical cross-section

for this process is $\sigma_{t\bar{t}} = 6.7 \pm 0.8$ pb for $m_t = 175$ GeV/c^2 [11]. Top quarks can also be produced at the Tevatron via $q\bar{q'} \rightarrow tb$ and $qg \rightarrow q'tb$ through the weak interaction. The cross section for these processes is lower (3pb) and the signal is much more difficult to isolate as backgrounds are much higher.

The top quark is predicted to decay almost exclusively into a W-boson and a bottom quark ($t \rightarrow Wb$) [11]. The total decay width $t \rightarrow Wb$ is $\Gamma = 1.50$ GeV [11]. This corresponds to an incredibly short lifetime of 0.5×10^{-24} seconds. This happens so quickly that hadronization and bound states do not take place, which leads to the interesting consequence that the top quark spin information is passed to the decay products [3].

Because top quark production and decay is dominated by $p\bar{p} \rightarrow t\bar{t} \rightarrow WbWb$, three channels dominate the final state of top quarks at the Tevatron:

- (12%) $t\bar{t} \rightarrow W^+bW^-\bar{b} \rightarrow (\bar{l}v_l b)(l'\bar{v_{l'}}\bar{b})$ [1]
- (44%) $t\bar{t} \rightarrow W^+bW^-\bar{b} \rightarrow (q\bar{q'}b)(\bar{v_l}l\bar{b}) + (\bar{l'}v_{l'}b)(q''\bar{q'''}\bar{b})$
- (44%) $t\bar{t} \rightarrow W^+bW^-\bar{b} \rightarrow (q\bar{q'}b)(q''\bar{q'''}\bar{b})$

The final state quarks in these processes hadronize and manifest themselves as showers of neutral and charged particles called jets. Unfortunately, it is difficult to distinguish between jets produced from different flavor of quarks. The consequence of this is that it becomes much more difficult to distinguish different processes in the detector. It is possible to distinguish bottom quarks. This a critical component of identifying top quark events, which we will discuss in detail in chapter 3.

The three top quark decay channels are generally called the dilepton, lepton plus jets, and all-hadronic. In this thesis, we will concentrate on the detection and reconstruction of the lepton plus jets channel. The Feynman diagram of the lepton plus jets channel is

[1] (') denotes different flavor

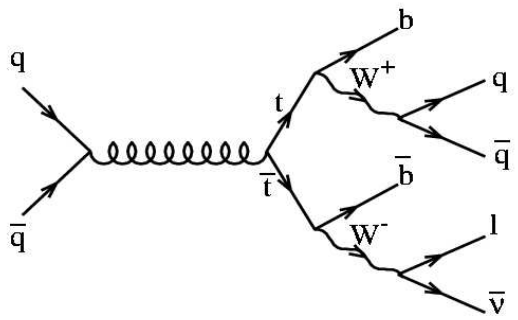

Figure 1.1: Lepton Plus Jets Diagram

shown in Figure 1.1.

Very few properties of the top quark have been measured, and even fewer have been measured with great accuracy. Only the top mass is known with any relative certainty. Measurements of the properties of the top quark are important tests of the Standard Model, but also interesting probes into new phenomena. These include searches for exotic decay modes, as through a charged Higgs boson $t \rightarrow Hb$ [4], and new production mechanisms, perhaps through a new heavy neutral gauge boson [9].

Symmetries play an important role in characterizing the behavior of elementary particles. A "symmetry" is an invariance of a physical system under transformation of the independent variables. In general, a symmetry implies a conservation law. For example, the invariance of the description of a physical system to linear translations of its spatial coordinates is associated with the conservation of linear momentum. Since the transformation can be over a continuous range of values, this is called a continuous symmetry.

A "discrete" symmetry involves a "swap" between fixed choices in certain variables. Three discrete symmetries of great importance in particle physics are:

- Charge Conjugation (C)
  - Transformation of particles to anti-particles.

  - Invariance implies conservation of charge.

- Parity (P)
  - Transformation of of coordinates to negative coordinates ($\vec{x} \rightarrow -\vec{x}$).
  - The physical system is invariant under mirror reflection.

- Time Reversal (T)
  - Transformation of time ($t \rightarrow -t$) in all expressions.
  - Invariance implies the physical process is reversible.

In 1955, W. Pauli showed that any plausible field theory is invariant under the product of these three transformations, CPT [5]. Indeed, each symmetry separately seems intuitive, and initially, physicists believed that they were separately conserved. This changed in 1957 with C.S. Wu's Nobel prize winning experiment with radioactive nuclei [7]. Wu measured an asymmetry in the angular distribution of electrons in beta decay, proving that weak interactions do not conserve parity. Next, in 1964, Cronin, Firth, and collaborators showed that the weak interactions also violated the product CP [6]. By virtue of Pauli's CPT theorem, they therefore also violate T. Time reversal has now been shown to be violated in the measurement of an asymmetry in the decay of kaons and anti-kaons at the CPLEAR experiment [8]. Charge conjugation is known to be violated in weak interactions by the lack of observation of right-handed neutrinos or left-handed anti-neutrinos.

Although the weak interaction is a "symmetry violator", the strong interaction is currently believed to respect C,P, and T. However, there is very little test of this at high energies. Top quark physics at the Tevatron offers an interesting new forum for the study of discrete symmetries in the strong interaction. It is a strong process at very high energy.

As will be shown in this thesis, we can completely reconstruct the $t\bar{t}$ kinematics, which enables the study of charge flow on a per event basis. With the charge in hand, we can define two charge asymmetries:

$$A_C = \frac{N_t(p) - N_{\bar{t}}(p)}{N_t(p) + N_{\bar{t}}(p)} \tag{1.1}$$

$$A_{fb} = \frac{N_t(p) - N_t(\bar{p})}{N_t(p) + N_t(\bar{p})} \tag{1.2}$$

where $N_i(j)$ = is the number of particle i traveling in the direction of particle j

- A_C is charge symmetry; a non-zero value for this implies a net top current flowing along the proton direction.
- The front-back asymmetry, A_{fb}, is the difference in the number of top quarks flowing forward and backward along the proton direction. This kind of asymmetry is typically associated with parity-violating weak production processes. This is not expected in strong interactions, though new production mechanisms that violate parity such as a Z' particle or Top Color could appear as a front back asymmetry in top production [9] [10]. If we assume that CP symmetry is conserved then $N_{\bar{t}}(p) = N_t(\bar{p})$ and the charge asymmetry is equal to the front back asymmetry.

Curiously, although the strong interaction conserves C, QCD predicts that strong interactions produce a net charge asymmetry in the pair production of top quarks at the Tevatron. Evaluated at leading order, heavy flavor pair production via $q\bar{q}$ or gg does not discriminate between quark and anti-quark. But at next-to-leading order, radiative

corrections involving a virtual or real gluon in $q\bar{q} \to Q\bar{Q}$ lead to a difference in the production of Q and $\bar{Q}$, and consequently a charge asymmetry. The asymmetry originates from interference between initial and final state gluon brehmsstrahlung processes, shown in Figures 1.2a and 1.2b, which produce a negative asymmetry, and the "box diagram" with the Born processes shown in Figures 1.2c and 1.2d, which produce a positive asymmetry. The overall charge asymmetry is positive and predicted to be between $4-5\%$ by Kuhn and Rodrigo [29], and 3.8% by next-to-leading order Monte Carlo generator MC@NLO [17]. In this analysis we assume CP symmetry is conserved and therefore, the front-back asymmetry will be equal to the predicted charge asymmetry.

In this thesis, we present the measurement of A_{fb} in $t\bar{t}$ production, using 695 pb^{-1} of $p\bar{p}$ collision data collected at the CDF experiment. We first isolate a sample of top events and understand their backgrounds. We then develop a method to reconstruct the $t\bar{t}$ kinematics, and use it to measure the production angle of the top quark, the angle between the top quark and the proton beam. The top quark production angle is defined as:

$$\Theta = Tan^{-1}\left(\frac{P_t}{P_z}\right) \tag{1.3}$$

where P_z and P_t are the longitudinal and transverse momentum of the top quark in a coordinate system where the proton beam is the z-axis. The production angle distribution for the top quark, as predicted by the Monte Carlo simulation MC@NLO, is shown in Figure 1.3. The production angle is used to define and count the number of forward (in the proton direction) and backward (against the proton direction) events in the sample, and thus measure A_{fb}. The measured production angle is distorted from its true value by a number of experimental complications. Corrections for these effects are applied to the

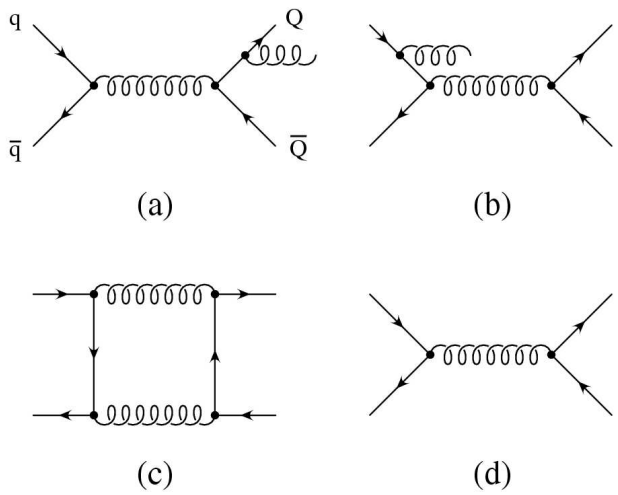

Figure 1.2: NLO Diagrams

forward and backward counts to produce a measurement of A_{fb} which can be compared to the theoretical prediction. We now explain the experiment and method of measuring A_{fb} in detail.

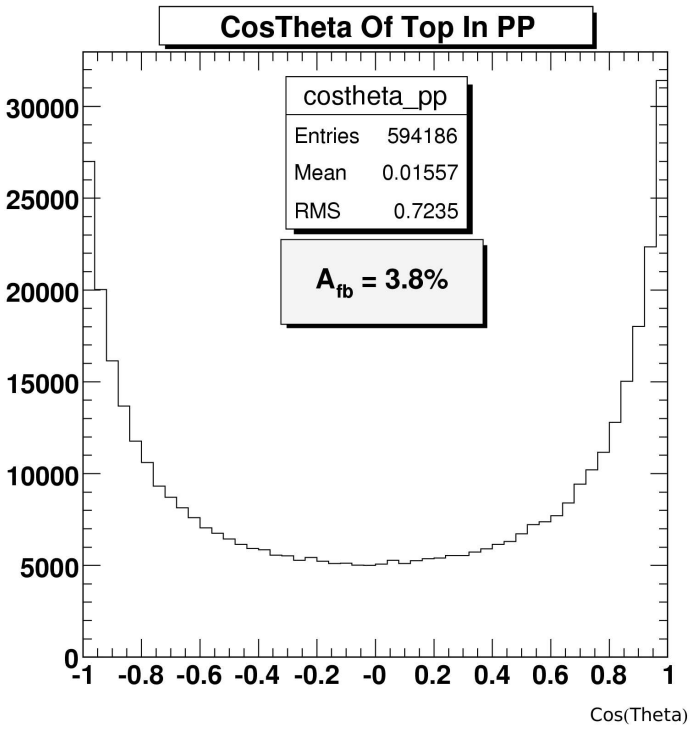

Figure 1.3: $Cos(\Theta)$ Distribution MC@NLO

CHAPTER 2

Experimental Apparatus

2.1 The Tevatron

The Tevatron is a superconducting synchrotron that can accelerate and store high energy beams of protons and anti-protons [27]. Thirty six bunches of protons circle the ring clockwise as thirty-six antiproton bunches circle counter-clockwise. The beams are steered to collide at two places along the ring, which is where the detectors are placed. These collisions occur at a center of mass energy of 1.96 TeV. Each of the thirty six bunches contain roughly ten billion protons squeezed into a volume 57 cm long and 70 microns in diameter. Bunches circle the 6 km ring roughly 50,000 times a second. Even with such a high crossing rate and dense collection of particles, there is no guarantee that there will be an interaction. The Tevatron achieves, on average, only a single interaction per bunch crossing. The rate and energy of collision completely determine the spectrum of particles available to detection.

A simple schematic of the facility is shown in Fig. 2.1. The first stage of acceleration begins at a Cockcroft-Walton accelerator. Inside this device, hydrogen atoms are ionized with an extra electron to produce H^-. The hydrogen ions are then accelerated with a static electric field to 750 KeV and passed to a linear accelerator. The linear accelerator is approximately 500 feet long and consists of cascaded radio frequency cavity resonators

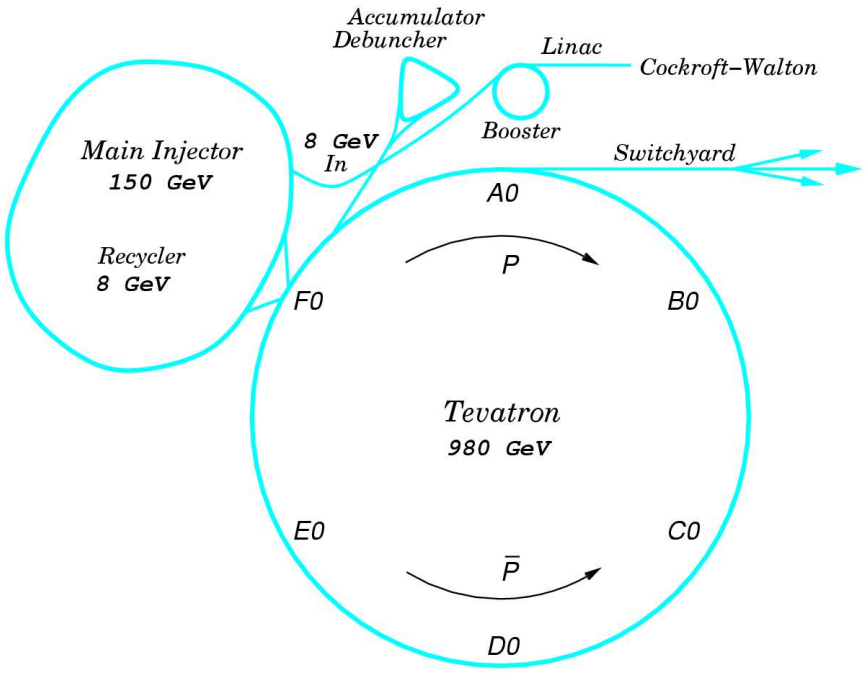

Figure 2.1: The Tevatron Accelerator Chain.

that accelerate the ions. The cavities operate with a phase delay so that as the ion bunch passes through an accelerating force is always present. At end of the linear accelerator the beam of ions has enough energy (400 MeV) and is stable enough so that the electrons can be stripped off, leaving only a beam of protons. A carbon foil strips the electrons away but leaves the heavy proton beam intact.

The next device in the sequence is the booster. The booster is a circular accelerator that creates bunches of protons by collecting them in a synchronized way from the linear accelerator: each proton bunch actually consists of several shots of protons from the linear accelerator. The protons experience an acceleration with each revolution in the booster as they pass through a series of RF cavities. After circling the booster roughly 20,000 times, the final energy of the protons before entering the next stage, the main injector, is 8 GeV.

The main injector is a synchrotron like the Tevatron. It serves four functions: it accelerates the proton bunches from 8 GeV to 150 GeV, it provides 120 GeV protons for anti-proton production, it transfers anti-protons from the anti-proton source, and it injects protons and anti-protons into the Tevatron.

To produce anti-protons, 120 GeV protons from the main injector are diverted into a nickel target. An incredible array of different particles are created from the collision, some of which are anti-protons. A lithium lens is used to focus the particles that appear after the collision, and a magnet is used to separate the anti-protons from the other particles. This process produces about 1 anti proton per 100,000 protons. After the magnetic filter, the antiprotons have a very randomized spread of energy. To produce a tightly confined high energy beam there must be little spread in energy between particles in the bunch. The anti-protons exiting the magnetic filter enter a debuncher which "cools" the beam so that the spread in energy is not so large. Anti-protons are then collected from the debuncher in the accumulator where they are accelerated to 8 GeV and stored as more anti-protons are created. The debuncher continuously feeds anti-protons into the accumulator, creating bunches, in a process called "stacking". This is generally the rate determining step in the entire process of producing $p\bar{p}$ collisions. It can take up to 12 hours to produce the necessary amount of anti-particle bunches. Once the accumulator has produced enough anti-protons they are injected back into the main injector, accelerated to 150 GeV, and then both proton and anti-protons bunches are injected into the Tevatron.

Thirty-six proton and thirty-six anti-proton bunches are injected into and circulate in opposite directions in the Tevatron. They are accelerated up to an energy of 980 GeV by a series of RF cavities that span a small portion of the 6 km circumference of the Tevatron. The orbits are helical, and arranged so that the beams only cross at two points, where the D0 and CDF detectors are placed.

The ability of a collider to produce collisions is quantified by the instantaneous luminosity $\mathcal{L}$ [11]:

$$\mathcal{L} = n \cdot f \cdot \frac{N_p N_{\bar{p}}}{4\pi\sigma_x\sigma_y} \quad cm^{-2}s^{-1} \tag{2.1}$$

where n is the number of bunches, f is the revolution frequency for a single bunch traveling at the speed of light (50 kHz at the Tevatron), N_p and $N_{\bar{p}}$ are the number of protons and anti-protons per bunch, and σ_x and σ_y represent the average transverse width of the bunch. The rate with which an event occurs is then $\mathcal{L} \cdot \sigma$, where σ is the cross-section of a process.

On average, the Tevatron has operated with the following parameters over the last year:

n	36 Bunches
f	50 kHz
N_p	225e9
$N_{\bar{p}}$	40e9
σ_x	36 μm
σ_y	36 μm

Table 2.1: Tevatron Parameters

Plugging these numbers into equation 2.1 leads to an instantaneous luminosity of 80e30 $cm^{-2}s^{-1}$. This is initial luminosity that the beam has when reaching a steady state in the Tevatron.

The luminosity exponentially decreases with time as the beam degrades due to collisions between protons and anti-protons. While the Tevatron is colliding beams, the accumulator stacks anti-protons to prepare for the next re-initialization of colliding beams. As stated earlier, stacking takes about 12 hours. On average, the luminosity of the colliding beams reduces to about 10e30 $cm^{-2}s^{-1}$ before the new anti-protons are ready to be

injected. To maximize integrated luminosity it is best to inject the new set of protons and anti-protons as soon as possible so that the luminosity of the beam is kept at a maximum.

2.2 The Collider Detector Facility (CDF)

The results of the $p\bar{p}$ collisions are recorded with the CDF detector. A graphical representation of CDF is shown in Figure 2.2. The CDF detector weighs about 5,000 tons and stands roughly three stories high [28]. The beam pipe runs through the center of the detector and the components of the detector are arranged around it in cylindrical layers. The innermost layer of the detector utilizes silicon micro lithography to make recordings of the trajectory of charged particles' close to the interaction point. Outside the silicon, the coverage of charged particle tracking is extended by a large barrel-shaped wire chamber. The silicon detector and the wire chamber are enclosed in a large solenoid. The curved motion of charged particles in the magnetic field can be used to measure the particles momentum. Electromagnetic calorimeters are placed on the outside of the tracking chamber followed by hadronic calorimeters. The calorimeters detect and measure energy carried by electrons, photons, and hadrons. A large slab of steel separates the calorimeters from several wire chambers placed on the very outside of the detector. The outer wire chambers detect muons, which are the majority of particles that pierce the steel slab. Figure 2.3 describes how different particles appear in the sequential layers of detector. Each individual detector will be discussed in detail in following sections, but first the coordinate system at CDF is introduced.

2.2.1 Coordinate System At CDF

The detector is described by right-handed spherical coordinates where the z-coordinate points along the direction of the proton beam, and the x-coordinate points out radially within the plane of the Tevatron ring. The polar angle, Θ, is often transformed to a

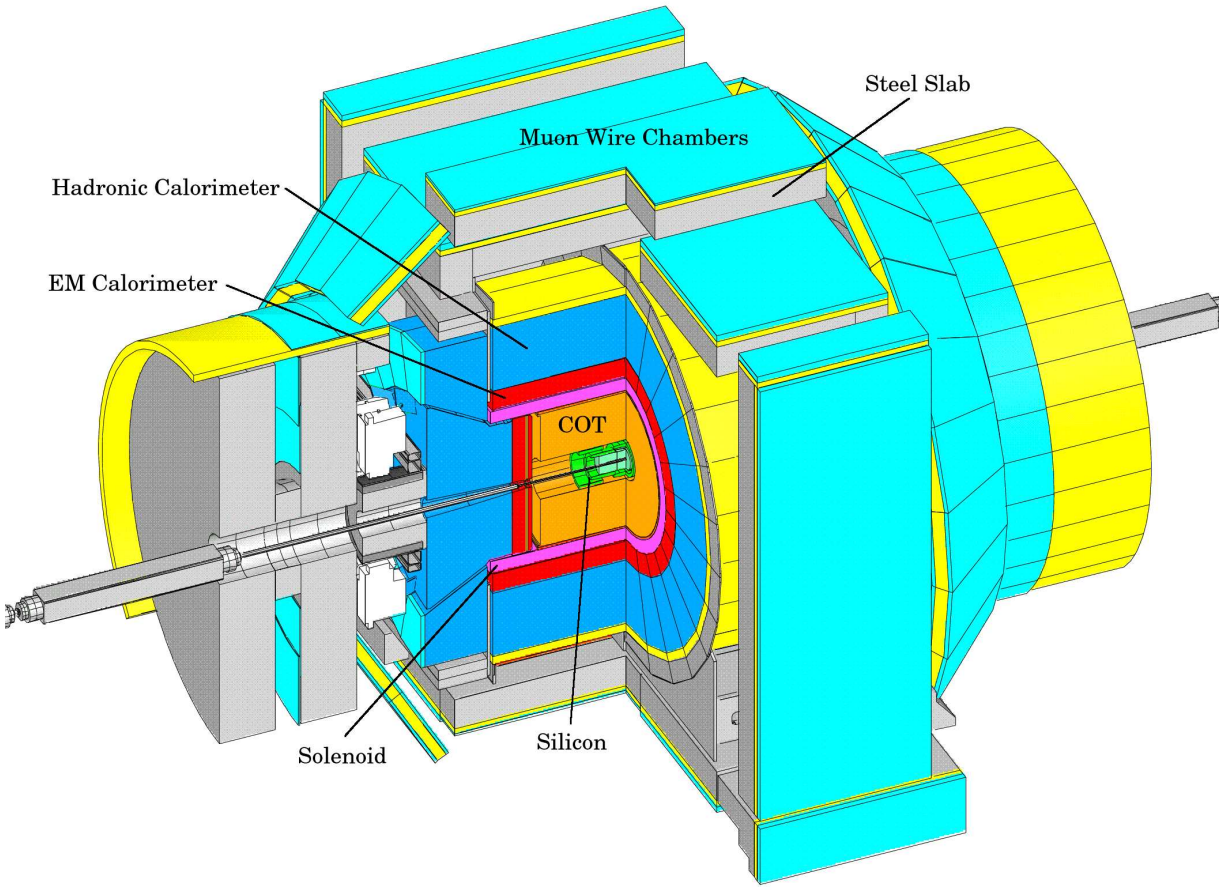

Figure 2.2: CDF

quantity called pseudo-rapidity which is defined as:

$$\eta = -log\left(tan\left(\frac{\Theta}{2}\right)\right) \tag{2.2}$$

2.2.2 Silicon Tracking

The silicon detectors consist of sequential lines of p-n junctions that detect the presence of charged particles that deposit ionization in the depletion region of the semiconductor. The position of the ionization can be localized with very high precision, and linking them together provides an accurate reconstruction of charged particle trajectory.

CDF has three different silicon-based detectors: Layer 00 (L00), the Silicon Vertex

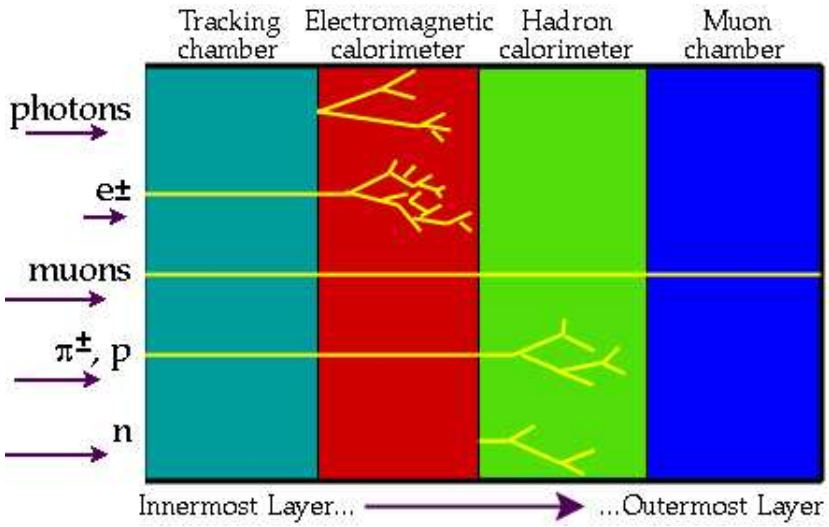

Figure 2.3: How Different Particles Look In The Detector

Detector (SVX), and the Intermediate Silicon Layer (ISL) covering a radial range 1.5cm to 32cm from the center of the beam pipe. A cross-sectional view of the silicon detectors is shown in Figure 2.4 and a longitudinal view in Figure 2.5. The three sections of the silicon detector together provide coverage of tracks with $\eta < 2.0$.

L00 is a single sided, radiation hard, silicon microstrip detector. It is the first layer of silicon detector immediately outside the beam pipe. Outside of L00 is the SVX which consists of five layers of double sided silicon ladders arranged like concentric barrels. One side of an SVX silicon wafer provides information in the $r - \phi$ plane and the other side in the $r - z$ plane. This allows for 3-dimensional tracking in the SVX. Outside of the SVX is the last layer of silicon detector, the ISL, which consists of double sided silicon arranged like barrels. The ISL has one layer that covers the central region of the detector and two more that extend out to $\eta = 2$. This improves tracking in the forward part of the detector, beyond the coverage of the central outer tracker (COT) which is discussed next.

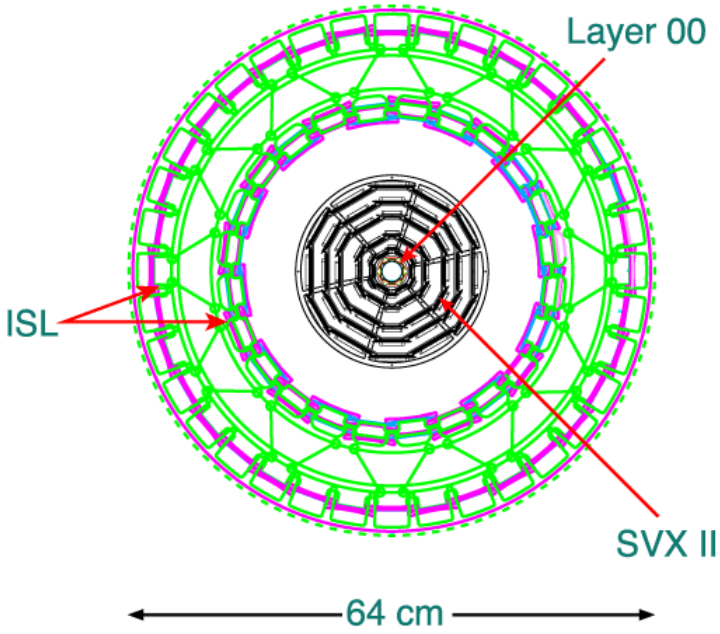

Figure 2.4: Cross-section of silicon detectors

2.2.3 Central Outer Tracker (COT)

The COT is an open cell drift chamber designed to measure the three dimensional trajectories of charged particles with $\eta < 1.0$. The COT is made up of eight concentric layers of cells, illustrated in Figure 2.6, filled with a 50-50 mixture of argon and ethane gas. Each cell, which spans the entire length of the COT, contains twelve *sense wires* that alternate with thirteen *potential wires*, illustrated in Figure 2.7. The potential wires run at a positive high voltage (2 kV) and the sense wires run slightly higher (3 kV). Gold-Mylar panels that make up the sides of each cell are run at ground potential.

As a charged particle passes through a cell, the gas mixture is ionized along the particles trajectory. The ions in the gas drift towards the sense wires due to the electric field. The magnetic field from the outer solenoid and the electrostatic potential in the cell shapes the drift trajectory of each particle, shown in Figure 2.8. As the electrons approach the

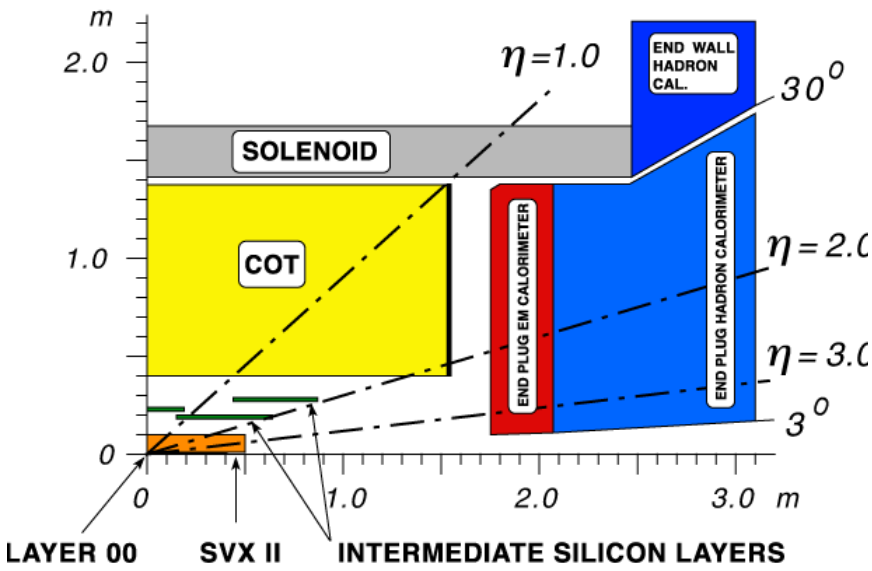

Figure 2.5: Side view of CDF

sense wire, they ionize more atoms, creating an avalanche effect. The charge is deposited on the sense wire and the total charge and arrival time is recorded.

The eight super-layers of the COT alternate between layers where the wires in each cell are parallel to the z-axis, and where the wires are 3° offset from the z-axis. Cells with parallel wires provide $r-\phi$ information and offset cells provide $r-z$. Three-dimensional tracks are reconstructed by a least squares fit of a helix from the $r-z$ and $r-\phi$ information from wire hits. The curvature of the helix is used to calculate the momentum of the charged particle. The transverse momentum resolution is $\delta Pt/Pt = 0.003 \cdot P_t$ for COT standalone track reconstruction and $\delta P_t/P_t = 0.0012 \cdot P_t$ for COT combined with silicon tracking.

2.2.4 Solenoid

The COT is surrounded by a superconducting solenoid. The solenoid is built from Al-stabilized NbTi superconductor and cooled with liquid helium. It operates with a current of about 4650 Amps and provides a 1.4 Tesla magnetic field along the z-axis uniform

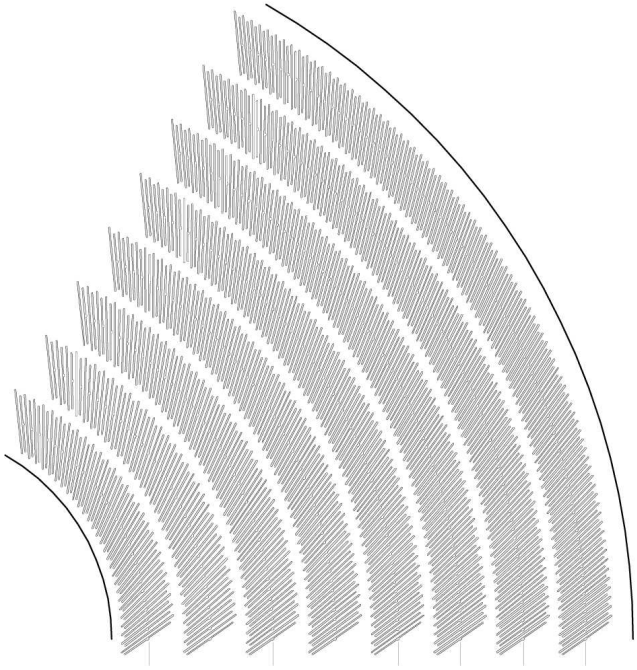

Figure 2.6: 1/6th view of the COT end plate

within 0.1%.

2.2.5 Electromagnetic Calorimeters

The electromagnetic (EM) calorimeters, which sit directly outside the solenoid, detect energy deposited by electrons and photons. The EM calorimeters are divided into two sections: the central EM calorimeter (CEM) which covers a range η <1.1 and the plug EM calorimeter (PEM) which covers 1.3< η <3.6. The EM calorimeters are made up of alternating layers of scintillator and lead. Electrons that enter the EM calorimeter radiate photons (brehmsstrahlung) from deceleration in the coulomb field of the lead atomic nuclei. The radiated photons convert into electron positron pairs which then also brehmsstrahlung. This cascade effect produces a shower of electrons and positrons that enter the scintillating material which emits a light pulse proportional to the number of electrons. The light from all scintillating layers is collected in waveshifters and sent along light pipes to photomultipliers. Wave-shifters are used to shift the light from blue to

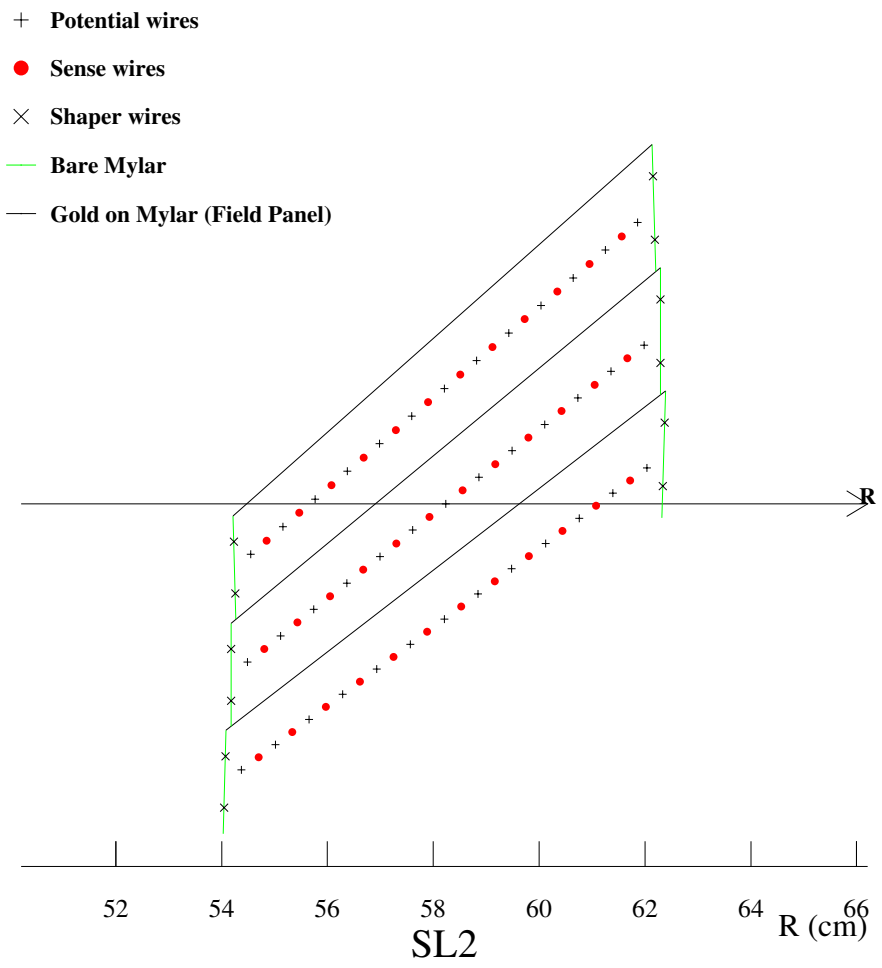

Figure 2.7: Cell layout for a COT super-layer

green where photomultiplier tubes are most sensitive. The integrated light received from the photomultiplier tubes is proportional to the total number of electrons that passed through the scintillators. The number of electrons is proportional to the energy of the initial particle. The energy measurement is therefore a "counting measurement" and its uncertainty goes like $\sqrt{N} \propto \sqrt{E}$.

The EM calorimeters are approximately 18 radiation lengths deep. Electrons and photons will be totally absorbed, but charged hadrons, which do not radiate, will only

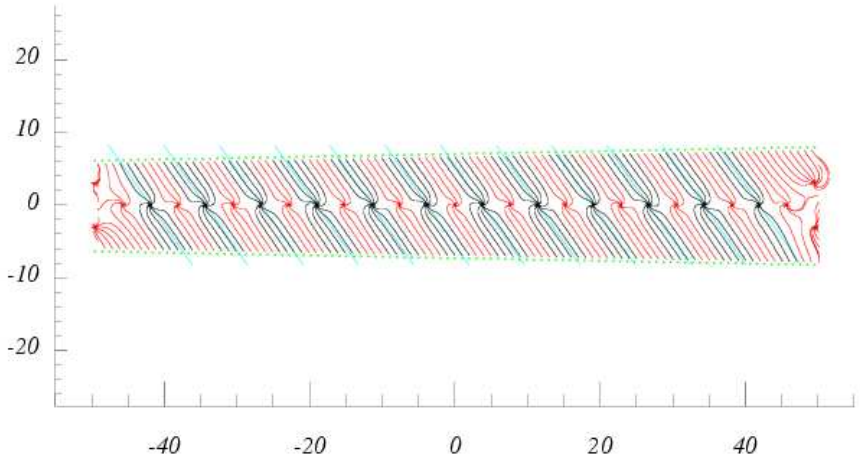

Figure 2.8: Drift trajectory for a COT cell

loose a small portion of energy in the EM calorimeter. Hadrons will deposit energy in the hadronic calorimeters that sit just outside the EM calorimeters. This allows the energy deposited by photons and electrons to be distinguished from that deposited by hadrons.

The central electron strip (CES) is a layer of wire chambers embedded in the EM calorimeter at the depth of "shower maximum". The CES localizes the shower position inside the large calorimeter cell. A diagram of a single calorimeter wedge is shown in Figure 2.9.

Isolated electrons are used to measure the energy resolution of the EM calorimeter towers by comparing transverse energy measured in the calorimeters to the transverse momentum measured in the tracking chamber. The EM calorimeters at CDF are found to have an energy resolution of $\sigma_{E_T} = 0.135 \cdot \sqrt{E_T}$ GeV

2.2.6 Hadronic Calorimeters

The hadronic (HAD) calorimeters sit directly outside the EM calorimeters with the exact same angular coverage. The HAD calorimeters consist of alternating layers of scintillator and iron. Charged hadrons that enter the HAD calorimeter eventually undergo

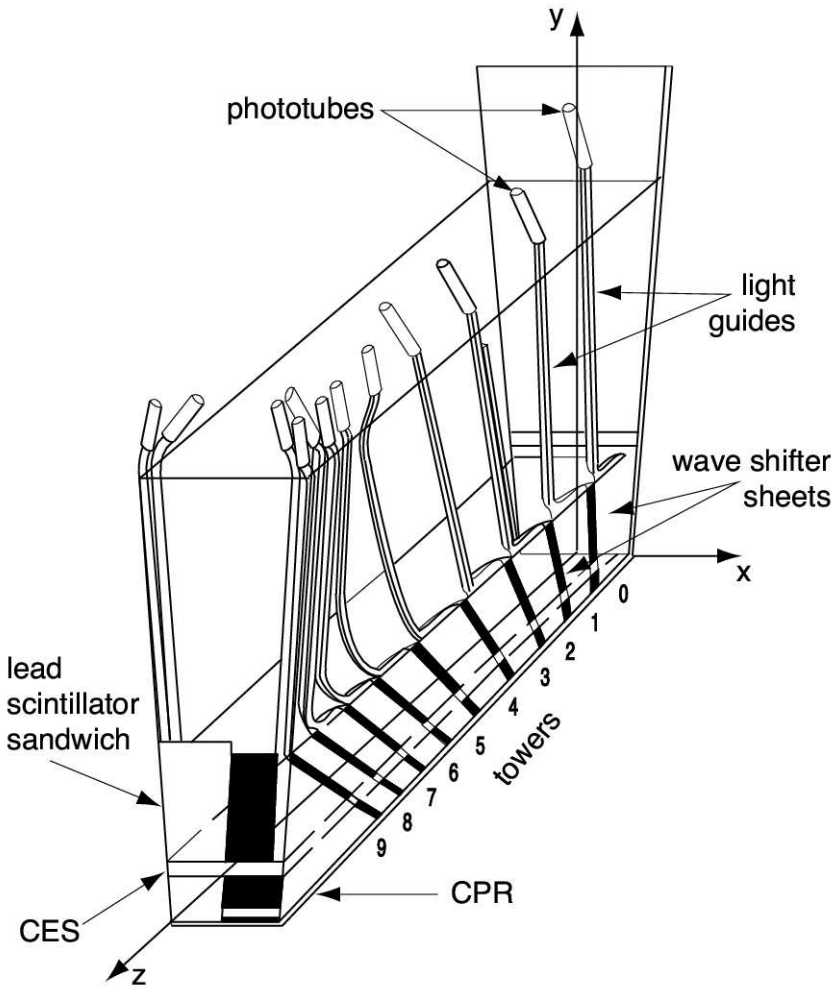

Figure 2.9: EM Calorimeter Wedge

a nuclear interaction, creating high energy debris that collide with atoms in the iron and split the iron nuclei. The debris from the nuclei can undergo further interactions. The cascade of hadrons enters scintillating material which emits a light pulse proportional to the number of hadrons. The light pulse is waveshifted from blue to green and fed outwards to phototubes. Because the measurement depends on nuclear collisions, which are far more improbable then electron brehmsstrahlung as in EM Calorimeters, the HAD calorimeters have to be much longer to contain the shower. Because the number of interactions is smaller they have a poorer resolution. The HAD calorimeters at CDF have

an energy resolution of $\sigma_{E_T} = 0.75 \cdot \sqrt{E_T}$ GeV.

2.2.7 Muon Chambers

A steel slab encompasses the calorimetry and tracking chambers, as seen in Figure 2.2. The calorimeters and this steel serve to stop almost all particles, except for muons, which are very penetrating. Wire chambers, placed just outside the steel, detect these muons. The hits in the muon wire chambers define a track or stub, which can be matched to a track reconstructed in the COT. Figure 2.10 demonstrates a layer of muon chamber cells.

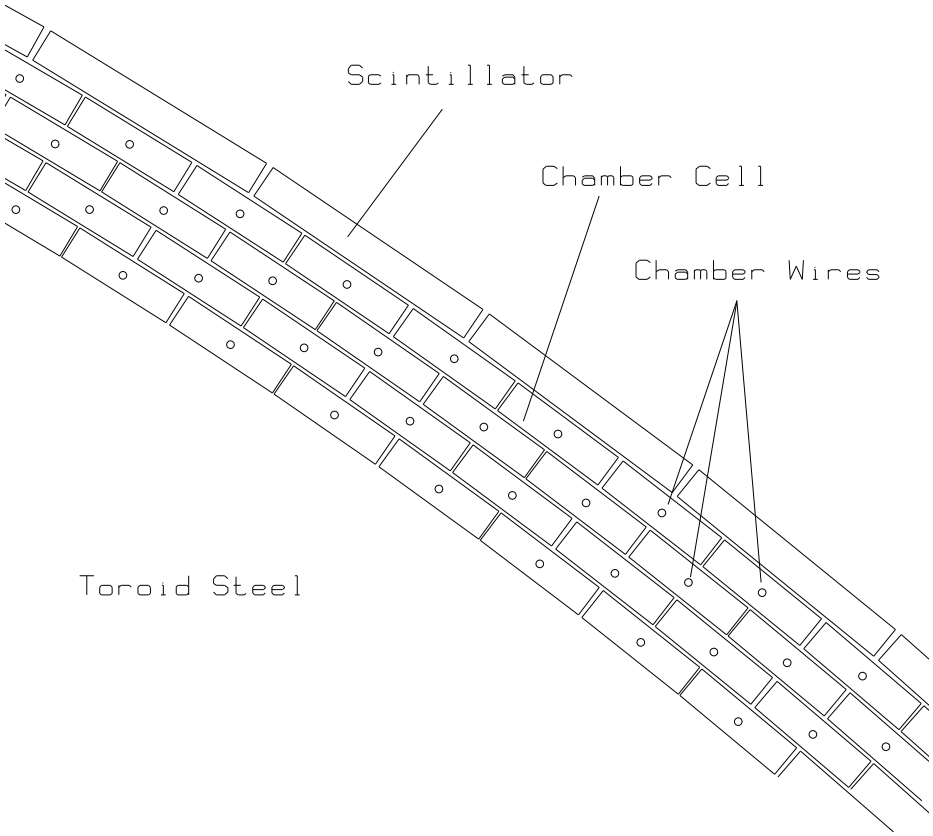

Figure 2.10: Cells in a muon chamber

CDF has three sets of muon wire chambers, the central muon detector (CMU), the central muon upgrade (CMP), and the central muon extension (CMX). These chambers

contain drift cells which detect charge particles in a similar manner as cells in the COT. They each consist of four layers of cells stacked radially with a small azimuthal offset to aid in reconstructing hits in the chamber to tracks in the COT. The angular coverage of CMU,CMP, and CMX is shown in Figure 2.11. The CMP chambers are outside the CMU separated by another steel slab. A muon which leaves signals in both the CMU and CMP are referred to a a CMUP muon. The CMX extends the η coverage of the muon chambers to 1.0.

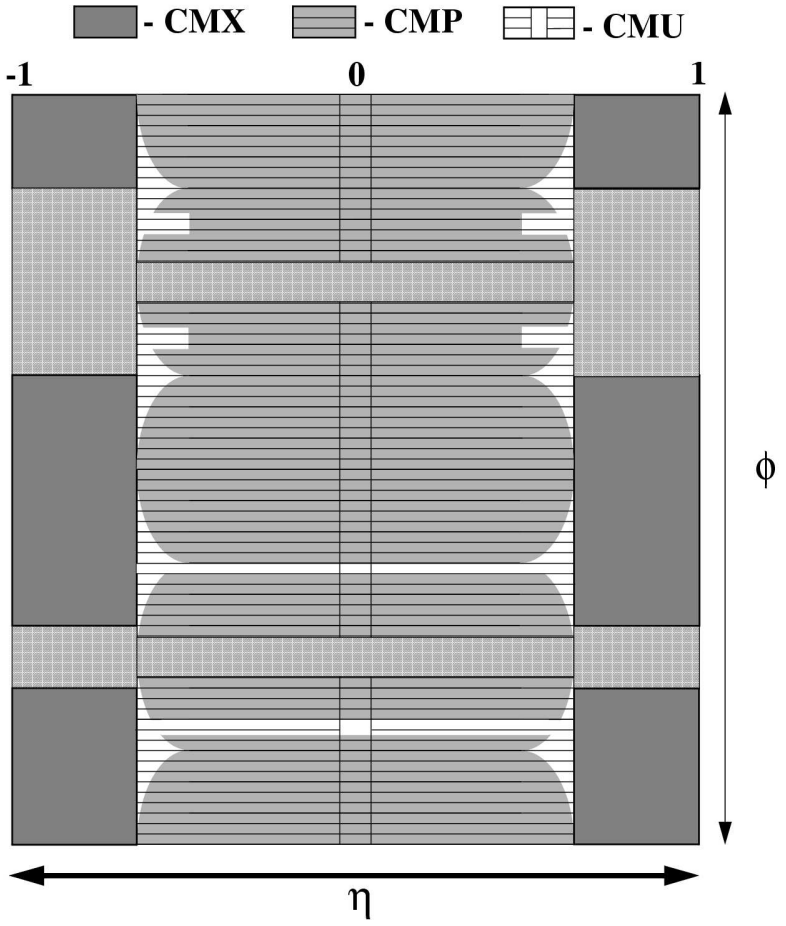

Figure 2.11: Angular coverage of CMU,CMP, and CMX

2.3 Data Acquisition System

Proton and anti-proton bunches in the Tevatron collide inside the CDF detector every 396 nano-seconds. The amount of information provided by the detector in each collision is impossible to record at such a high rate. A decision system or trigger is required to select events of most interest. Three tiered decision stages, called trigger levels, are used to scrutinize each event. Each level has more detail, but takes more time. If an event passes all three trigger levels it is recorded to tape. An outline of the trigger system and decision flow is shown in Figure 2.12.

2.3.1 Level 1 Trigger

The L1 trigger is a buffered system that stores events for 42 crossings before making a decision. Each event is stored inside the buffer for 5500 ns. This time is sufficient to collect signals from all detector systems, particularly the long drift times in the muon systems. The level one trigger makes a decision in less than 4000 ns, therefore no event must be dropped because of a long decision time in the level one system. Three systems at L1 one run parallel to examine an event: the eXtremely Fast Tracker (XFT), the calorimeter trigger boards (DIRAC), and the muon trigger cards. The XFT does a fast reconstruction of tracks in the COT and matches these tracks to energy depositions in towers of the calorimeters or hits in the muon chambers. DIRAC cards calculate the energy deposited in calorimeter towers and sum the energy deposited in all towers to estimate the amount of missing transverse energy. Muon trigger cards reconstruct tracks in the muon chamber. Information from all three systems is used to determine whether an event is passed to Level 2.

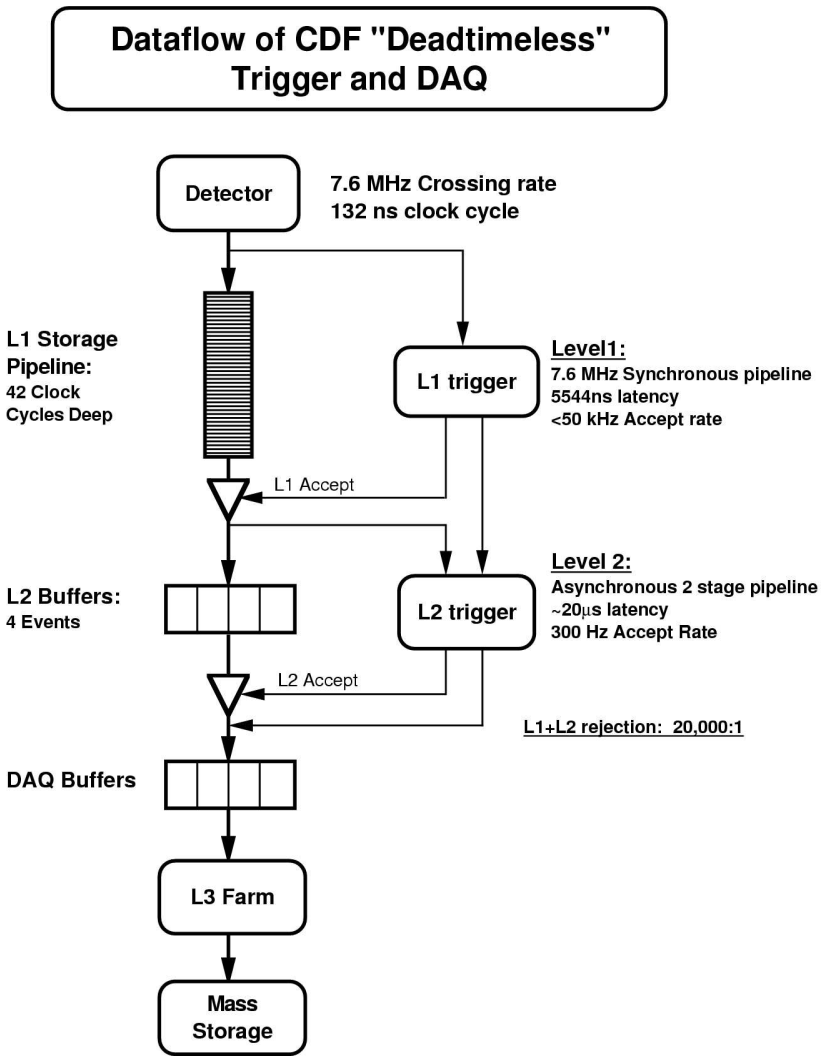

Figure 2.12: Dataflow of CDF trigger and DAQ system

2.3.2 Level 2 Trigger

Information from events that pass L1 is passed to one of four buffers in the L2 system. Events remain in the buffer until a decision is made. Four systems are used to process events: the silicon vertex tracker (SVT), calorimeter boards (DCAS), calorimeter shower maximum (XCES), and muon hit and track data. The SVT reconstructs tracks in silicon and measures the impact parameter of these tracks. DCAS is used to find clusters of hadrons and electromagnetic showers to reconstruct jets. XCES is used to identify photons

and electrons using the COT and EM calorimeters. Muon hit and track information is utilized to provide further level of detail about an event. The information is passed to processors that can combine the information and make trigger decisions based on programmable settings.

2.3.3 Level 3 Trigger

A L2 trigger initiates a full read out of the event through the DAQ system. The event data is passed to a PC farm where a complete version of the offline reconstruction is performed. The L3 trigger decision is then made based on the particle content and event topology. An accepted event is sent to a mass storage system.

CHAPTER 3

Event Selection

The $p\bar{p}$ collisions at the Tevatron produce a broad range of final states. This analysis is performed with $t\bar{t}$ events in the lepton plus jets channel. The lepton plus jets channel is characterized by a high P_t lepton, a large amount of missing energy, and at least four jets from two b-quarks and two quarks from the hadronic decay of a W-boson. These are relatively rare events, and their isolation from the general collision data requires a detailed selection.

The event selection is performed through several stages. The first stage is performed in real time, as the online trigger selects collision events for readout. Since leptons have such distinct signals, our primary trigger selections are based upon the detection of a high momentum electron in the CEM, or a muon in the CMUP or CMX. The trigger requirements are described in the electron and muon identification sections below. Events passing the online trigger requirements are written to disk in separate "streams" for each trigger. The streams are processed offline to apply calibration constants and fully reconstruct higher level signals such as tracks and showers from low level detector information. Tracks and showers are then combined into "physics objects" such as muon, electron, and jet candidates, which are examined for quality and form the essential part of the $t\bar{t}$ selection.

We first describe the separate selections for electron, muons, jets, and missing energy and then how these are combined to select $t\bar{t}$.

3.1 Electron Identification

A high momentum electron detected at the trigger level is used as a source for a possible $t\bar{t}$ lepton plus jets event. Electrons are identified as a single isolated track pointing to an isolated deposit of energy in a single electromagnetic calorimeter tower in the CEM ($|\eta| < 1.0$).

The trigger level requirements are listed first, followed by offline requirements for electron identification.

3.1.1 Triggers

Level 1

- A cluster of energy in the central EM calorimeters with $E_t \geq 8.0$ GeV.
- The ratio of energy deposited in the HAD compartment to EM compartment in the calorimeter tower is small [(HAD/EM) ≤ 0.125] as expected for an electromagnetic shower.
- One or more tracks in the COT with $P_t \geq 8$ GeV.

Level 2

- A cluster of energy in the central EM calorimeters with $E_t \geq 16.0$ GeV, and (HAD/EM) ≤ 0.125.
- A track in the COT at level 1 must point to the cluster.
- Matching track $P_t \geq 8$ GeV.

Level 3

- A cluster of energy in the central EM calorimeters with $E_t \geq 18.0$ GeV, and (HAD/EM) ≤ 0.125.
- Matching track $P_t \geq 8$ GeV.
- $L_{shr} < 0.4$

  The lateral shower profile compares the small sharing of the shower energy across neighboring towers with expectations based on test beam data. The L_{shr} cut is on the χ^2 of the comparison.

3.1.2 Offline Selection

Offline selection is applied to events that have passed through the trigger levels. The cuts can be more stringent because the offline information is more detailed. Electrons that pass the offline selection criteria are referred to as "tight" electrons. The offline selection criteria for electrons is detailed below.

- $E_t \geq 20$ GeV

  Electrons in $t\bar{t}$ events are expected to have high energy.

- $P_t \geq 10$ GeV

  For an ideal electron $P_t = E_t$.

- $P_t \geq 50$ GeV (if $E_t > 100$ GeV)

  This cut filters out high momentum hadrons that fake electrons.

- $E_{HAD}/E_{EM} < 0.055 + 0.00045 \cdot E$

  Since the electromagnetic shower of an electron is mostly contained in the electromagnetic compartment, we can reduce the number of jets misidentified as an electron by requiring that the ratio of hadronic energy to electromagnetic energy is small.

The requirement is linearly scaled with energy because very high energy electrons will deposit a larger fraction of energy into the hadronic compartment.

- $E/p < 2.0$ (if $E_t < 100$ GeV)

  The energy an electron deposits in the calorimeter should be approximately be the same as the momentum of the matching track.

- # COT Axial Segments ≥ 3 and # COT Stereo Segments ≥ 2

  This is a quality cut on the electron track found in the COT.

- $Track|z_0| < 60$ cm

  z_0 is the z intercept of the electron track. This is done to guarantee the track originates from optimal regions in the COT.

- $-3.0cm < Q \cdot \Delta x < 1.5$ cm

  Δx is the distance in the x-coordinate between the COT track position extrapolated to the CES and the actual hits in the CES chamber. Matching tracks between CES and the COT is charge dependent and, therefore, this cut is different depending on the charge of the electron track.

- $|\Delta z| < 3.0$ cm

  Δz is the distance in the z-coordinate between the COT track position extrapolated to the CES and the actual hits in the CES chamber. A minimum window is applied to this distance to match the COT track to the CES hits.

- $\chi^2_{strip} < 10$

  A χ^2 test is performed between the profile of hits in the CES and the expected profile of electrons.

- $L_{shr} < 0.2$

  A tighter requirement on the lateral shower profile.

- $Isolation < 0.1$

  The energy deposited in a calorimeter by an electron is very collimated. An "isolation" requirement examines the energy nearby the electron. Jets that fake electrons are filtered out by requiring that energy deposited in a cone around the electron is small. This is quantified by the variable I_l.

$$I_l = \frac{\sum E_t^{\Delta R<0.4} - E_t^{electron}}{E_t^{electron}} \tag{3.1}$$

  The ratio of energy in a cone $\Delta R = \sqrt{(\Delta\phi)^2 + (\Delta\eta)^2}$ around the electron to the energy of the electron must be smaller then 0.1.

- No Conversions

  High energy photons interacting with material in the detector can convert into electron-positron pairs. Electrons from conversions are backgrounds to our electron selection. High energy conversions appear as oppositely charged tracks traveling in the same direction and having a pair mass of zero. An electron identified with a conversion partner is rejected.

3.2 Muon Identification

A high momentum muon detected at the trigger level is used as a source for a possible $t\bar{t}$ lepton plus jets event. Muons are identified as tracks in the COT matched to stubs in the muon chambers.

3.2.1 CMUP Triggers

Level 1

- A muon stub in the CMU detector with $P_t \geq 6.0$ GeV.
- Track with $P_t \geq 4$ GeV in the COT extrapolates to the muon stub.
- An additional stub required in the CMP detector.

Level 2

- COT track with $P_t \geq 8$ GeV

Level 3

- Tracks in the COT are extrapolated to stubs in both the inner CMU and outer CMP
- COT track with $P_t \geq 18$ GeV

3.2.2 CMX Triggers

Level 1

- A muon stub in the CMX detector with $P_t \geq 6.0$ GeV
- $P_t \geq 8$ GeV COT track with hits in at least four superlayers

Level 2

- No Level 2 Trigger Selections

Level 3

- COT track extrapolates to CMX stub
- COT Track with $P_t \geq 18$ GeV

3.2.3 Offline Selection

- $P_t \geq 20$ GeV

  Muons originating from W-bosons are expected to have large momentum.

- E_{EM} <Maximum of 2.0 GeV or $2.0 + 0.0115 \cdot (p - 100.0)$ GeV

  Muons are minimum ionizing particles and therefore should leave little energy in the electromagnetic calorimeters. A linear correction term is added because the deposited energy increases slightly with the momentum of the muon.

- E_{HAD} <Maximum of 6.0 GeV or $6.0 + 0.0115 \cdot (p - 100.0)$ GeV

  Muons should leave little energy in the hadronic calorimeters as well, though slightly more energy then the EM calorimeters because of the increased amount of material.

- $\Delta x_{CMU} < 3.0$ cm

  For an event with CMU hits, the extrapolated COT track must be within a small window of the hits in the CMU chamber.

- $\Delta x_{CMP} < 5.0$ cm

  For an event with CMP hits, the extrapolated COT track must be within a small window of the hits in the CMP chamber.

- $\Delta x_{CMX} < 6.0$ cm

  For an event with CMX hits, the extrapolated COT track must be within a small window of the hits in the CMX chamber.

- $|d_0| < 0.02$ cm with hits in silicon

  The impact parameter, d_0, is the distance of closest approach from the track to the

z-axis. This rejects cosmic rays and mis-reconstructed tracks that do not apparently originate from the primary vertex.

- $|d_0| < 0.2$ cm without any hits in silicon

  This requirement is made less stringent if the track cannot be matched to a corresponding one in silicon or if the silicon detector is not in operation.

- $Track|z_0| < 60$ cm

  z_0 is the z intercept of the muon track. This is done to guarantee the track originates from optimal regions in the COT.

- # COT Axial Segments ≥ 3 and # COT Stereo Segments ≥ 2

  This is a quality cut on the muon track found in the COT.

- COT exit radius < 140 cm (CMX Only)

  This is done for muons detected in the CMX chambers only. It imposes a requirement that the track from the muon left in the COT had passed through a minimum number of COT layers before matching to the CMX chamber.

- Isolation < 0.1

  As in the case of the electron, the "isolation" requirement examines the energy nearby the muon. Jets with muon "punchthrough" or decays in flight are rejected by requiring that energy deposited in the calorimeters in a cone around the muon is small. The isolation of the muon is the ratio of the energy in a cone around the muon to the momentum of the muon.

$$I_l = \frac{\sum E_t^{\Delta R<0.4}}{P_t^{muon}} \tag{3.2}$$

- Cosmic Veto

  Cosmic rays detected by CDF are characterized by two back-to-back tracks separated with a $\Delta\phi$ very close to 180 degrees and timing of the hits such that the track appears to be going "backward in time" across half of the COT diameter. These characteristics can be flagged and such muons are rejected.

3.3 Jet Identification And Corrections

Partons produced in the $p\bar{p}$ collision will hadronize into a shower of neutral and charged particles. This shower of particles is referred to as a jet. The signature of a jet is multiple tracks from the charged particles and a large amount of energy deposited in both hadronic and electromagnetic calorimeters. Jets are identified as isolated deposits of energy in the calorimeters. The energy and direction of the jets are found by associating energies deposited in neighboring calorimeter towers into a single calorimeter "cluster".

The clustering is performed around any tower with $E_t > 3.0$ GeV. For any such tower, the algorithm begins by adding the energy of all towers within a cone of $\Delta R < 0.4$ of the highest energy tower in the group. The center of the cluster is calculated as the energy weighted centroid of the tower coordinates. A reclustering is then performed around this new center and then the process repeated until it converges. The energy of the jet is the sum of the energy in a cone $\Delta R < 0.4$ around the center. Once a tower is included inside a clustered jet, it is no longer allowed to be included in the clustering of any other jet.

Several corrections to calculated jet energies account for known issues with the calorimeter response and other sources of deposited energy. Corrections are applied to jets in "levels", each of which is described below.

- Level 1 (η Dependence): Applied to the raw energy deposited in the calorimeter to correct for differences in calorimeter response as a function of η.

- Level 2 and 3 are no longer in use.
- Level 4 (Multiple Interactions): Energy from an overlapping $p\bar{p}$ interaction during the same bunch crossing will be detected inside jet clusters, increasing the energy of the measured jet. This correction subtracts that contribution on average.
- Level 5 (Absolute): Corrects the jet energy measured in the calorimeter for any non-linearity and energy loss in the un-instrumented regions of each calorimeter.
- Level 6 (Underlying Event): The underlying event is defined as the energy associated with the spectator partons in a hard collision event. These are the partons that do not contribute to the hard scattering, but whose peripheral interaction produces low energy particles in the event. Depending on the details of the particular analysis, this energy needs to be subtracted from the particle-level jet energy.
- Level 7 (Out Of Cone): The choice of $\Delta R < 0.4$ for clustering is arbitrary. Some of the jet energy will be outside of this cone. This correction uses Monte Carlo models of jets to correct for the out-of-cone energy, taking the jet energy back to the parent parton energy.

For this analysis, all jets are corrected to level 4 for selection purposes and to level 5 for all other purposes.

For the purpose of $t\bar{t}$ identification, jets are grouped into two kinds: "tight" and "loose". Any jet with level 4 corrected $E_t \geq 15.0$ GeV and $|\eta| < 2.0$ is a tight jet, and any jet with level 4 corrected $E_t \geq 8.0$ GeV and $|\eta| < 2.0$ is considered a loose jet. Note that tight jets are a subset of loose jets.

3.4 Missing Energy

At the Tevatron, the protons and antiprotons in the beam have zero transverse momentum and therefore, the 4-vector sum of the transverse energy in the detector should be zero. In a lepton plus jets event, a large amount of momentum is carried away by the undetected neutrino. This produces a transverse momentum inbalance in the detector, which is called missing energy ($\not\!\!E_T$), and it is closely related to the neutrino transverse momentum.

The calculation of $\not\!\!E_T$ begins as the negative of the vector sum of the raw (uncorrected) transverse energy in the calorimeter towers broken into x,y components.

$$\not\!\!E_{T,x}^{raw} = -\sum_{towers} E^{tower} \cdot Cos(\phi_{tower}) \tag{3.3}$$

$$\not\!\!E_{T,y}^{raw} = -\sum_{towers} E^{tower} \cdot Sin(\phi_{tower}) \tag{3.4}$$

Since the neutrino causes the inbalance, it will be opposite the apparent total momentum, thus the minus sign in the above equations.

In the case that the event contains a muon, which leaves minimal energy in the calorimeter, the sum is corrected by subtracting the associated calorimeter energy and adding the muon track momentum (for events without a muon, this step is skipped).

$$\not\!\!E_{T,x}^{muon-corr} = \not\!\!E_{T,x}^{raw} - P_t^{muon} \cdot Cos(\phi_{muon}) \tag{3.5}$$

$$\not\!\!E_{T,y}^{muon-corr} = \not\!\!E_{T,y}^{raw} - P_t^{muon} \cdot Sin(\phi_{muon}) \tag{3.6}$$

Finally the effect of the jet corrections is incorporated by removing the raw jets and adding the corrected jets to the sum.

$$\not\!\!E_{T,x}^{L4-corr} = \not\!\!E_{T,x}^{muon-corr} + \sum_{loose\ jets} E_{raw}^{jet} \cdot Cos(\phi_{jet}) - \sum_{loose\ jets} E_{L4Corrected}^{jet} \cdot Cos(\phi_{jet}) \tag{3.7}$$

$$\not\!\!E_{T,y}^{L4-corr} = \not\!\!E_{T,y}^{muon-corr} + \sum_{loose\ jets} E_{raw}^{jet} \cdot Sin(\phi_{jet}) - \sum_{loose\ jets} E_{L4Corrected}^{jet} \cdot Sin(\phi_{jet}) \tag{3.8}$$

The final corrected $\not\!\!E_T$ vector has magnitude equal to the quadrature sum of the x-y components and angular direction calculated from the x-y components.

$$\not\!\!E_T = \sqrt{(\not\!\!E_{T,x}^{L4-corr})^2 + (\not\!\!E_{T,y}^{L4-corr})^2} \tag{3.9}$$

$$\phi_{\not\!\!E_T} = Tan^{-1}(\not\!\!E_{T,y}^{L4-corr} / \not\!\!E_{T,x}^{L4-corr}) \tag{3.10}$$

3.5 Secondary Vertex b-Tagging

Top quarks decay to Wb, but most background processes to $t\bar{t}$ do not contain heavy flavor quarks in the final state. The bottom quark is long lived, and the typical b from top decay, with $p = 65$ GeV, travels a distance $\gamma\beta c\tau = 500$ μm. This can be observed in the silicon detector as tracks within a jet forming a secondary vertex that is displaced from the primary vertex. An algorithm, called SecVtx, identifies events displaced secondary vertices in jets, and these vertices are used in selection to reduce background processes [12] [13]. A jet identified with a secondary vertex by SecVtx is said to be "tagged".

Tagging is performed for each jet in an event by selecting quality tracks inside the jet and searching for vertices formed by those tracks. The quality of a track is determined

by the number of hits in silicon tracking, the χ^2 of the track, and the momentum of the track. Good tracks with a large impact parameter are tested to see if they form a common vertex. For each vertex found, the length of the vector pointing from the primary vertex to the secondary vertex in the $r-\phi$ plane (L_{xy}), is calculated along with its error ($\sigma_{L_{xy}}$). If $L_{xy}/\sigma_{L_{xy}} > 3.0$ the jet is "tagged".

3.6 Dilepton Veto

To separate the $t\bar{t}$ lepton plus jets channel from the dilepton channel, any event with a second tight lepton is removed.

3.7 Z veto

Events are removed if a tight lepton and a second object form an invariant mass consistent with a Z-boson ($76 < M_{ll} < 106$ GeV). If the tight lepton is an electron, the second object must be an isolated electromagnetic object, a reclustered jet with 95% of energy deposited in the electromagnetic calorimeter, or an opposite-signed isolated track. If the tight lepton is a muon, the second object must be an isolated muon or an opposite-signed isolated track.

3.8 Primary Vertex Reconstruction

The origin of the event is the primary vertex. The z-position of the primary vertex is used to cluster jets and to ensure that leptons and jets belong to the same interaction. The z-position of the primary vertex is estimated by the error weighted sum of the z-intercept of all tracks within a common point of origin.

$$z_{PrimVertex} = \frac{\sum_{tracks} z_0^{track}/\Delta^2_{track}}{\sum 1/\Delta^2_{track}} \tag{3.11}$$

To ensure the lepton originates from the primary vertex events are rejected if the lepton z-intercept is not within 5 cm of the primary vertex z-position. This reduces the number of events in the sample where jets and the lepton are part of different interactions.

3.9 Summary Of Lepton Plus Jets Selection

A summary of the selection criteria for $t\bar{t}$ events is shown below. After the background processes are introduced, it will be shown that this set of selection requirements produces roughly a 4 to 1 signal to background ratio.

- One tight high-P_t lepton as described in sections 3.1 and 3.2

  First criteria for selection, which occurs at both trigger level and offline.

- Dilepton veto:

  Separates lepton plus jets from dilepton events.

- Z veto:

  Reduces the amount of background with Z-bosons.

- Primary vertex check:

  ensures the lepton and jets originate from the same process.

- $\not\!\!E_T \geq 20$ GeV:

  Selection based upon the presence of a neutrino in lepton plus jets events.

- ≥ 3 Tight and 1 Loose Jets:

  Reduces background by requiring the same number of jets as partons in a $t\bar{t}$ lepton plus jets event.

- ≥ 1 SecVtx "Tagged" jet:

  Rejects background processes without heavy flavor quarks present.

3.10 DataSet

For 695 pb^{-1} of data collected at CDF the number of events that pass through event selection is 257. The breakdown of those events among the three high P_t lepton triggers is shown in Table 3.10.

	CEM	CMUP	CMX
N_Events	154	72	31
$\%OfTotal$	60.0%	28.0%	12%

It is instructive to see how the top quark "signal" emerges from background as we apply the selection criteria of section 3.9 but allow events with any number of jets in the sample. This is illustrated in Figure 3.1, where the selected data sample and their predicted backgrounds are plotted as a function of "tight" jet multiplicity [14]. The black "points" represent the number of events in data, the yellow histogram represents the predicted $t\bar{t}$ signal, and all other histograms represent backgrounds. For events with one or two "tight" jets, background processes dominate the data sample. For a requirement of 3 "tight" jets or more, the top quark "signal" clearly emerges from the predicted background, and the predicted $t\bar{t}$ signal is consistent with the data.

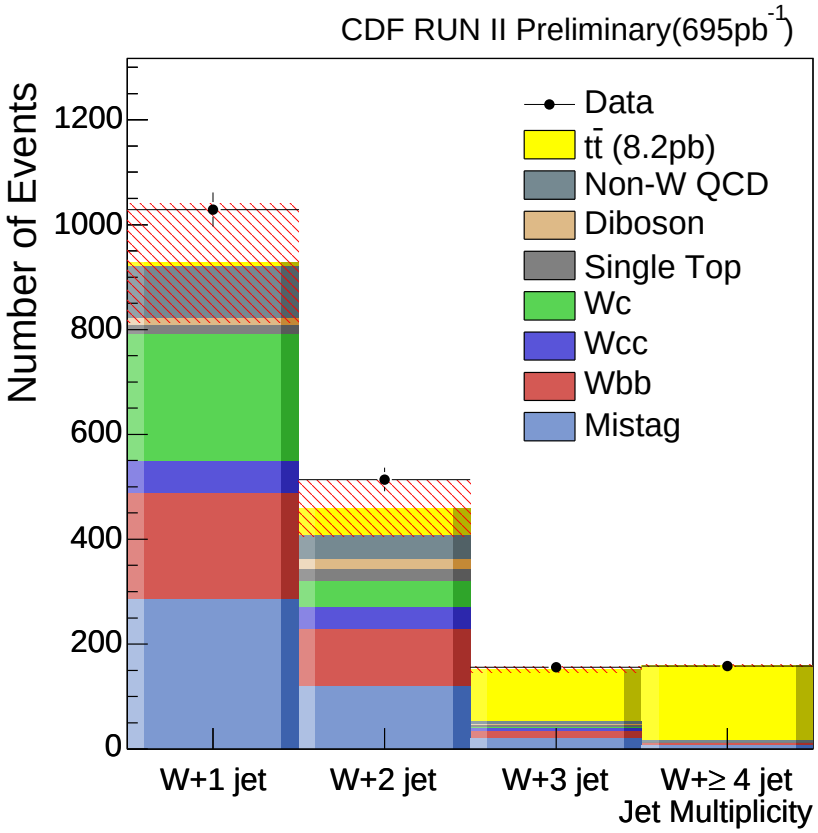

Figure 3.1: Top Quark Signal vs Jet Multiplicity

CHAPTER 4

Backgrounds

Several kinds of processes without top quarks slip past our selection criteria. These events are backgrounds to the top quark signal and their presence biases and dilutes the measurement. Background events can be grouped into five different categories based on the physics processes in the event: electroweak processes, single-top events, QCD, W-boson plus heavy flavor quarks, and W-boson plus light flavor quarks. The nature of these backgrounds and the techniques used to normalize each one are discussed below. The order of each discussion is based upon the fact that some backgrounds need to be understood in order to calculate others.

4.1 Electroweak

Several electroweak processes contribute to the total background. They are WW, WZ, ZZ, and Z$\rightarrow \tau\tau$ events. These processes compromise the selection criteria because each can produce a real lepton and neutrino, as well as a number of jets. The numbers in our sample are estimated using the theoretical cross section, the luminosity of the sample, and an overall selection efficiency derived from Monte Carlo simulation of the processes in question. Theoretical cross sections for these processes are shown in Table 4.1. The calculated number in our sample is given by

Process	Cross Section
WW	13.25 ± 0.25 pb
WZ	3.96 ± 0.06 pb
ZZ	1.58 ± 0.02 pb
Z→ $\tau\tau$	13.0 ± 1.5 pb

Table 4.1: Theoretical Cross Sections For ElectroWeak Backgrounds

$$N_{p\bar{p}\to X} = \sigma_{p\bar{p}\to X} \cdot \epsilon_{pretag} \cdot \epsilon_{tag} \cdot \int dt \cdot \mathcal{L} \tag{4.1}$$

where $\sigma_{p\bar{p}\to X}$ is the theoretical cross section, $\int dt \cdot \mathcal{L}$ is the total luminosity, ϵ_{pretag} is the pre-tagged selection efficiency derived from Monte Carlo, and ϵ_{tag} is the tagged selection efficiency shown in equation 4.2.

$$\epsilon_{tag} = \epsilon_{tag}^{MC} \cdot \Phi_{MC,data} \tag{4.2}$$

The tagged selection efficiency is derived from Monte Carlo, ϵ_{tag}^{MC}, multiplied by a scale factor, $\Phi_{MC,data}$, which represents the difference in tagging efficiency between Monte Carlo and data. The predicted number of events that pass event selection for the data sample is

$$N_{Events}^{EW} = 2.53 \pm 0.30$$

4.2 Electroweak Top Production "Single Top"

Single top quarks are produced at the Tevatron through two electroweak processes: a virtual W is created with energy to decay into a top quark and a bottom quark (s-Channel) or a virtual W interacts with a b-quark in the proton "sea" to produce a top quark (t-Channel). These processes are shown in Figure 4.1. Because these events contain

real top quarks, they may enter our sample, but they are backgrounds to our study of $t\bar{t}$ pair production. The single top background contribution is estimated similarly to the electroweak processes: from the theoretical cross section and luminosity as well as the selection efficiency derived from Monte Carlo. The theoretical cross-sections for single-top quark processes are shown in Table 4.2 along with the theoretical prediction for $t\bar{t}$ production [11]. The predicted number of events that pass event selection for the data sample is

$$N_{Events}^{EW} = 2.31 \pm 0.34$$

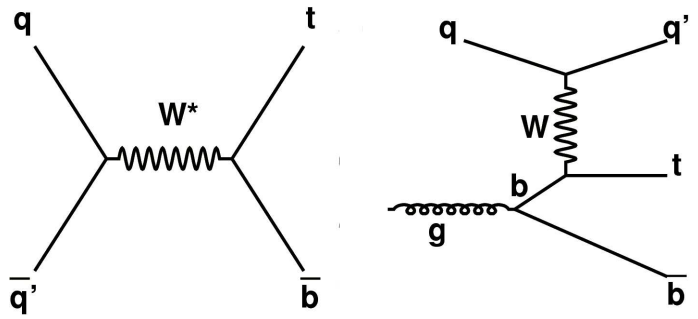

Figure 4.1: Single Top s and t Channel.

Process	Cross Section
$t\bar{t}$	6.7 ± 0.07 pb
Single Top - t Channel	1.98 ± 0.08 pb
Single Top - s Channel	0.88 ± 0.05 pb

Table 4.2: Theoretical Cross Sections For Top Production [11]

4.3 Pure QCD Backgrounds

By virtue of its richness and large cross sections, pure QCD can produce events which pass our selection by faking every aspect of $t\bar{t}$ events. These events can contain pairs of heavy flavor quarks $b\bar{b}$, $c\bar{c}$ as shown in Figure 4.2, light quarks, or gluon multi-jet events. They pass our selection by containing:

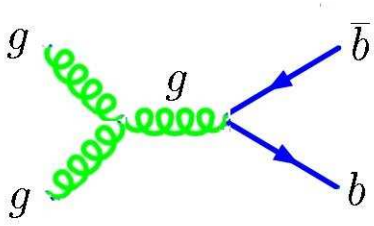

Figure 4.2: QCD Diagram.

- A fake lepton from a fragment of a jet, or a lepton from semi-leptonic decay of a bottom or charm quark.
- Mis-measured jets that produce an apparent signal of missing transverse energy ($\not\!\!E_T$).
- A b-tagged jet that comes from either a real heavy quark or mismeasured tracks faking a secondary vertex.

The probability of such a "total fake" event is small, but so many events are produced via strong interactions in hadron collisions that this process becomes a significant background.

Two variables most significantly separate QCD from $t\bar{t}$ events: missing transverse energy ($\not\!\!E_T$) and the isolation of the lepton (I_l) as defined in chapter 3. QCD events are expected to have low $\not\!\!E_T$ because there are no weak interactions that can produce a neutrino. The real or fake lepton, which comes from a jet, in QCD events is expected to be less isolated then other events since more tracks are expected to be close to the lepton. The QCD background is estimated directly from data by studying the sample events, before b-tagging, in the $\not\!\!E_T$ vs. lepton isolation plane. The $\not\!\!E_T$ vs. lepton isolation plane is divided into four regions:

- Region A: $\not\!\!E_T < 15GeV$ And $I_l < 0.2$
- Region B: $\not\!\!E_T < 15GeV$ And $I_l > 0.1$

- Region C: $\not\!\!E_T > 20GeV$ And $I_l > 0.2$
- Region D: $\not\!\!E_T > 20GeV$ And $I_l < 0.1$ (Signal Region)

The signal region is D. Region A and B are dominated by QCD events. It is assumed that the fraction of events that pass an isolation cut is uncorrelated with $\not\!\!E_T$. Therefore, the fraction of QCD events in the signal region can be estimated by:

$$F_{QCD,notag} = \frac{B}{A} \cdot \frac{C}{D} \tag{4.3}$$

The fraction of QCD events in the "b-tagged" signal region is estimated in two ways. In the first method, the same techniques as the pre-tagged sample is used, except that the isolation cut is set to 0.1 for all regions to improve statistics. The QCD fraction is:

$$F^1_{QCD,tag} = \frac{B^{tag}}{A^{tag}} \cdot \frac{C^{tag}}{D^{tag}} \tag{4.4}$$

Unfortunately, because b-tagging is so good at rejecting background, this method suffers from lack of statistics. To boost statistics, a second technique uses the pretag estimate and rescales by the expected tag rate, which is taken from region B.

$$F^2_{QCD,tag} = F_{QCD,notag} \cdot D \cdot \frac{B^{tag}}{B} \tag{4.5}$$

This assumes that the tag rate in region B is the same as in the signal region. Validation of this assumption has been performed by running Monte Carlo simulations of $b\bar{b}$ pairs.

The average value of the above two methods, $F^1_{QCD,tag}$ and $F^2_{QCD,tag}$ is used as the background prediction:

$$N_{QCD,tag} = \frac{F^1_{QCD,tag} + F^2_{QCD,tag}}{2} \tag{4.6}$$

The predicted number of events that pass event selection for the data sample is

$$N^{QCD}_{Events} = 12.37 \pm 2.92$$

4.4 W + Heavy Flavor ($Wb\bar{b}$, $Wc\bar{c}$, and Wc)

These background processes include a W boson produced in association with heavy quarks, as shown in Figure 4.3. The selection is compromised by a real lepton and neutrino from a W boson, a real bottom or charm quark, and the presence of other jets from higher order QCD processes.

The contribution of this background to our signal region is calculated by equation 4.7.

$$N_{W+hf} = (N_{pretag}(1 - F_{QCD}) - N_{EW} - N_{singletop} - N_{t\bar{t}}) \cdot f_{HF} \cdot \epsilon_{tag} \tag{4.7}$$

The number of events predicted in QCD, Electroweak, singletop, and $t\bar{t}$ is subtracted from the pretag sample, leaving an estimate for the number of events with a W-boson. The fraction of these events with heavy flavor quarks, f_{HF}, is calculated from a detailed Monte Carlo simulation Alpgen [19], which includes all possible processes contributing to the production of a single real W-boson. ϵ_{tag} is the tagging efficiency as defined in equation 4.2. f_{HF} and ϵ_{tag} are calculated for $Wb\bar{b}$, $Wc\bar{c}$, and Wc separately, which define the rates for each of these processes. Only the heavy flavor fraction relies on Monte Carlo, the absolute normalization is derived from the pretag sample in data. The predicted number of events in our data sample that pass event selection for each type of heavy flavor background is

$$N_{Events}^{Wb\bar{b}} = 12.4 \pm 3.2$$

$$N_{Events}^{Wc\bar{c}} = 5.6 \pm 1.6$$

$$N_{Events}^{Wc} = 3.6 \pm 0.9$$

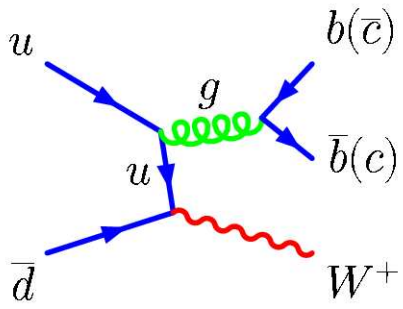

Figure 4.3: $Wb\bar{b}$ Diagram.

4.5 W + Light Flavor

The largest background to our b-tagged top selection is a set of processes containing no b-quarks at all: W plus light flavor jets. As in the W plus heavy flavor background, a real W boson exists providing a lepton and a neutrino. Light quarks or gluons produce the necessary high energy jets. The difference is that no bottom quark exists. A secondary vertex is mistakenly reconstructed when poorly reconstructed tracks seem to cross each other near the origin. A secondary vertex that does not originate from heavy flavor quarks is called a mistag.

Let the vector from the origin to the secondary vertex be $\vec{t}$ and the jet direction be $\hat{j}$. In a real secondary vertex, the flight path of the decaying particle $\vec{d}$ is in the direction of the jet, so that $\vec{t} = \vec{d} \cdot \hat{j} > 0$. In a sample of jets with no lifetime, the distribution of $\vec{t}$ for mistagged jets is found to be approximately symmetric around 0, and the apparent flight path of a mistag error is equally likely to appear as a positive or a *negative* lifetime. The

two cases of positive ($t > 0$) and negative ($t < 0$) flight path are shown in Figures 4.4 and 4.5. The secondary vertex tagging algorithm has been designed to keep the mistag rate low, at the level of approximately 0.5% of all jets.

In a high statistics sample with both real tags and mistags, the number of ($t < 0$) tags is a reasonable estimate of the number of mistags in the ($t > 0$) population. In our modestly sized sample the number of negative tags is small, and the implied measure of positive mistags has large statistical uncertainty. A better estimate of the positive mistag rate is derived by extrapolating into our sample the average mistag rate measured in very large inclusive jet samples.

The negative tag rate is found to be well parametrized by five jet variables (jet E_t, number of good SVX tracks, sum of all jet E_t in the event, jet η, jet ϕ) and measured in a very high statistics sample derived from triggers on 50 GeV jets. In any subsequent analysis this parametrization then gives the probability that a jet with given values of the tag parametrization variables will be negatively tagged. The negative tag probability of an event is taken to be the sum of the probabilities of all the jets in the event. Studies in large control samples derived from jet triggers with different energy thresholds (20 GeV, 75 GeV, 100 GeV) show good agreement between the prediction and the actual number of negative tags.

This technique is applied to estimate the number of events in our sample due to mistags in W + light flavor events. The predicted number of background events from W + light flavor (W+lf) processes is:

$$N_{W+lf} = N_{-}^{pred} \cdot \frac{N_{pre} - N_{pre}^{t\bar{t}} - N_{pre}^{QCD} - N_{pre}^{W+hf} - N_{pre}^{EW} - N_{pre}^{singletop}}{N_{pre}} \tag{4.8}$$

The predicted amount of $t\bar{t}$, QCD, W+hf, Electroweak, and single top background

events is subtracted from the total pretag sample leaving an estimate for the W+lf fraction. The predicted number of mistagged W+lf events is the W+lf fraction multiplied by the predicted amount of mistag events in the pretag sample. The predicted number of events that pass event selection for the data sample is

$$N_{Events}^{W+lf} = 14.8 \pm 2.1$$

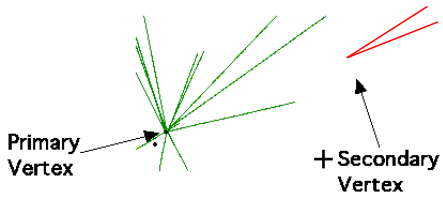

Figure 4.4: Positive Tag Vertex

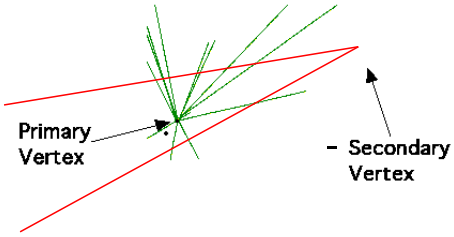

Figure 4.5: Negative Tag Vertex

4.6 Total Background Prediction

Using the methods described in the previous sections the predicted contribution for each background was calculated for an integrated luminosity of 319.5 pb^{-1} by several different members of the CDF Top Group. The data sample for this analysis consists of 695 pb^{-1} of integrated luminosity. Since we believe the background fraction is independent of luminosity, the background content for this dataset is estimated by scaling the predicted amount from 319.5 pb^{-1} to 695 pb^{-1}. The number of events in data that pass our selection criteria and the background estimates are shown in Table 4.3. For this analysis, we assume the number of top events is equal to the difference between data and the background estimate.

Table 4.3: Signal And Background Estimates For 695 pb^{-1}

Jet Multiplicity	3.5 Jet	4 Jet	$\geq$5 Jets
EW	1.46±0.24	0.85±0.17	0.22±0.07
SingleTop	1.29±0.28	0.89±0.20	0.13±0.02
QCD	4.34±1.57	6.70±2.31	1.33±0.85
W+LF Mistags	9.38±1.85	4.95±0.98	0.48±0.11
Wc	2.47±0.76	1.11±0.50	0.04±0.04
W$c\bar{c}$	3.75±1.31	1.77±0.87	0.04±0.04
W$b\bar{b}$	8.40±2.66	3.71±1.72	0.26±0.26
Total Bkg	31.09±5.35	19.99±3.99	2.51±0.94
Data	91	128	38
$t\bar{t}$ Pred.	59.9	108.0	35.5

CHAPTER 5

Modeling The Dataset

Models of the experimental dataset are used to simulate and understand our measurement. Generally, these models take the form of Monte Carlo simulations of the underlying physical process, called the "generator", and the response of the detector to that process, called the "CDF simulation". Information about both detector level objects, such as jets, and underlying physical objects, such as top quarks, is accessible in simulation. This allows comparisons between the elementary Standard Model objects and the objects actually observed at the detector level.

In chapter 4 we discussed the composition of the data set in terms of the signal and multiple backgrounds processes. Each physical process in the dataset is modeled by an appropriate simulation and normalized to the predicted number of events expected from the method described in chapter 4. The result is a complete model of the expected data collected at CDF and selected for this analysis. We discuss how the simulations are used and the tests we perform to verify their accuracy.

5.1 Models For Each Process

The simulation used for each signal or background processes is described separately below. For a few of the background simulations the selection criteria is modified to

Table 5.1: Summary Of Dataset Models

Process	Generator	N_{events} (Millions)
$t\bar{t}$	Herwig	2
W+lf	Herwig+Alpgen	2
W$b\bar{b}$	Herwig+Alpgen	2
W$c\bar{c}$	Herwig+Alpgen	2
Wc	Herwig+Alpgen	0.8
Single Top (S-Channel)	MadEvent+Pythia	0.8
Single Top (T-Channel)	MadEvent+Pythia	0.8
WW	Pythia	0.4
WZ	Pythia	0.4
ZZ	Pythia	0.4
Z$\rightarrow \tau\tau$	Herwig	0.4

improve statistics, but without changing predicted distributions. Table 5.1 is a summary of each process, the generator used, and the number of events created in that model. Each model is a complete simulation of the initial collision in the event, the final state particles, and the response of the detector. Kinematics and angular distributions for all particles in the simulated events are entirely available and, thus the event selection, reconstruction, efficiencies, etc. can be completely simulated for every process.

5.1.1 $t\bar{t}$ Signal

Two different generators are used to model $t\bar{t}$ signal events: Herwig and MC@NLO. Herwig generates events with a leading order matrix element calculation and uses a parton shower program to simulate gluon radiation and the showering of jets [16]. MC@NLO generates events with a next-to-leading order matrix element calculation [17]. It is used in conjunction with Herwig which performs the parton shower simulation. In this analysis, we use MC@NLO to model kinematics and angular distributions for $t\bar{t}$ events. MC@NLO provides a better model of higher order QCD processes, including the NLO charge asymmetry. Unfortunately, it is difficult at this time to create a large number of events simulated with MC@NLO and we currently have a sample of only 600,000 events with MC@NLO. Herwig is used to generate a large number of events, 2 million, for simulating

the effects that the detector, acceptance, and reconstruction have on the measurement. We expect these effects to be fairly independent of next-to-leading order effects, and by using Herwig for generation, the statistical error in the simulation of these effects is reduced by a factor of two.

5.1.2 Electroweak

Electroweak backgrounds are modeled by the Pythia Monte Carlo [15], which has a specialized treatment of final state hadronic interactions. Hard scattering processes are generated using Standard Model based calculations, and then a combination of analytical results and various QCD-string-based models simulate the multihadronic final states and parton evolution into jets.

5.1.3 Single Top

Single Top events are modeled at the generator level by MadEvent, for both s and t channels [18]. MadEvent is a multi-purpose, tree-level only event generator for a full range of collider processes including e^+e^-, ep, pp, $\gamma\gamma$, and $p\bar{p}$. It is a generator-only simulation and, therefore, is used in conjunction with Herwig to simulate parton showering into jets.

5.1.4 QCD

At this time, Monte Carlo simulations of QCD background events are not considered adequate models to predict the rare events that pass the $t\bar{t}$ selection. Instead, pretag data events with large $\not\!\!E_T$ and large lepton isolation (region C as described in section 4.3) are used as the model. Data events in this region are dominated by QCD and are assumed to be kinematically similar to background events in the signal region. Events in region C are required to have at least 3 tight jets and 1 loose jet and to boost statistics, instead of requiring a b-tagged jet, the jet with the highest positive mistag probability (as given by the mistag matrix, see section 4.5) is chosen as the b-tagged jet.

5.1.5 W + Heavy Flavor ($Wb\bar{b}$, $Wc\bar{c}$, and Wc)

W-boson plus heavy flavor events are modeled by Alpgen at the generator level and then passed to Herwig to simulate parton showering [19]. In W+jets events it is important to properly model the number of additional jets required by the selection criteria. Alpgen performs this accurately by including every diagram in a tree-level calculation. Herwig is used to simulate parton showering, but all of the other final state radiation effects in Herwig are turned off, so that the final state jet multiplicity is completely determined by the ALPGEN calculation.

5.1.6 W + Light Flavor

W-boson plus light flavor events are modeled by Alpgen at the generator level, with Herwig used to simulate parton showering. As in case of the W + heavy Flavor background, we use Alpgen to accurately treat the multiparton processes that generate additional jets. The selection criteria is modified by treating the most "taggable" jet, as described in chapter 3, as a "tagged" jet and not requiring an actual tag in the event.

5.2 Study Of Simulation Performance

As will become clear in chapter 7, we rely on our simulations to understand the corrections necessary to relate A_{fb} as measured to the fundamental A_{fb} in $t\bar{t}$ production. We must therefore verify that the simulation correctly models any intrinsic differences in the forward and backward response of the detector.

5.2.1 Primary Vertex

The primary vertex is the collision point of the $p\bar{p}$ interaction as measured from the center of the detector. If the position of the primary vertex in Monte Carlo simulation is drastically different than data, our model for the geometric acceptance of jets and leptons

will be skewed in η, and the production angle distribution of the top quark will not be simulated correctly.

In Figure 5.1, the primary vertex z-coordinate of simulated $t\bar{t}$ events are compared to primary vertex z-coordinate in the data used for this measurement. The background models are normalized as described in chapter 4 and the signal is normalized to the number of events found in the data minus the background prediction. The mean of the distribution for Monte Carlo and data are within statistical error, and the width differs by $< 4\%$. A slighly narrower distribution in the data is the result of a change in the beam profile since the production of the Monte Carlo. Although there is a slight shape difference, we believe that the overall agreement is good, and that the z vertex is adequately modeled for the analysis.

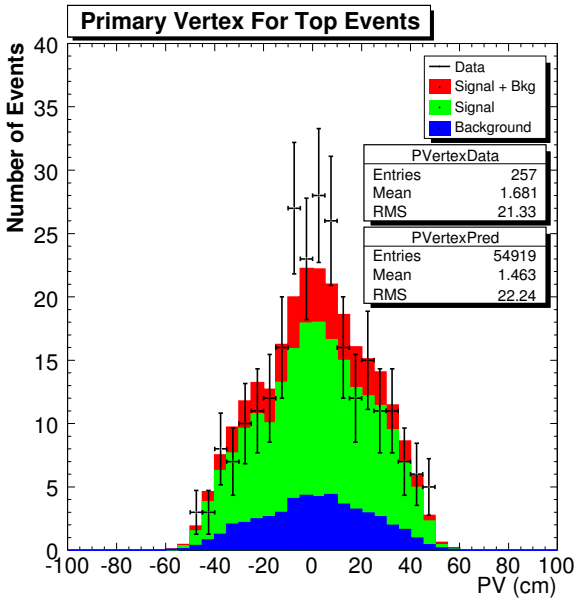

Figure 5.1: Primary Vertex z-coordinate for $t\bar{t}$ events

5.2.2 Front-Back Symmetry Of The Detector

The top event is composed of electrons, muons, and jets. Each of these is detected in a particular way, with particular apparatus. Therefore we can consider testing the simulation of electrons, muons, and jets separately to probe the modeling of the front-back acceptance of the detector. Fortunately, ideal samples are available in our high statistics inclusive high Pt lepton samples, which are dominated by leptonic vector boson decays. For example, $W \rightarrow e\nu$ events contain a high Pt electron and virtually nothing else. Comparing data and Monte Carlo for this process very selectively studies electron acceptance. With 70,000 identified $W \rightarrow e\nu$ decays, the η distribution of the electron can be compared to simulated $W \rightarrow e\nu$ decays with very good statistical precision over the entire detector, providing an accurate test of the simulation performance. We will examine the η distribution qualitatively, and also make a quantitative comparison. For our figure of merit, we will use A_{fb} where:

$$A_{fb} = \frac{N_{\eta>0} - N_{\eta<0}}{N_{\eta>0} - N_{\eta<0}} \tag{5.1}$$

and we will compare this A_{fb} between data and simulation. The samples of events for this test are selected from both Monte Carlo simulation and data with one isolated "tight" lepton, MET $>$ 20 GeV, zero "tight" jets, as described in chapter 3. It is assumed that there are very little or symmetric backgrounds to this selection criteria in collected data. The checks are performed with over 70,000 events for each check. For testing jets, the same method is applied, except a single tight jet is required in selection.

The results are shown in Table 5.2 and in Figures 5.2 to 5.7. The well known charge asymmetry from the vector boson production and decay is visible in the figures [20]. The asymmetry is opposite for positive and negative charged leptons, which demonstrates

charge-parity is conserved in the detector. Comparing data and simulation bin-by-bin in η, we see that the simulation maps the detector in detail. The total A_{fb}'s are consistent to a few parts in 1000, and within the very small statistical error of the measurement. This is certainly adequate for our measurement in a top quark sample of approximately 300 events.

Table 5.2: A_{fb} Check On ±CEM Electrons, ±CMUP,CMX Muons and Jets

Check	A_{fb} Monte Carlo	A_{fb} Data	Difference
+CEM Electron	0.082±0.003	0.081±0.003	0.001±0.004
-CEM Electron	-0.086±0.003	-0.088±0.003	0.002±0.004
+CMUP Muon	0.051±0.004	0.047±0.004	0.004±0.006
-CMUP Muon	-0.044±0.004	-0.052±0.004	0.008±0.006
+CMX Muon	0.115±0.006	0.113±0.006	0.002±0.008
-CMX Muon	-0.111±0.006	-0.131±0.005	0.02±0.008
Lead Jet	0.006±0.006	0.003±0.007	0.002±0.009

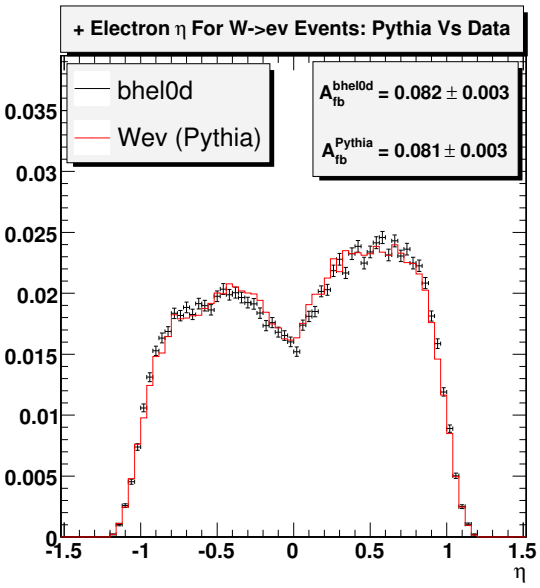

Figure 5.2: + Electron (CEM) η For W + 0 Jet Events

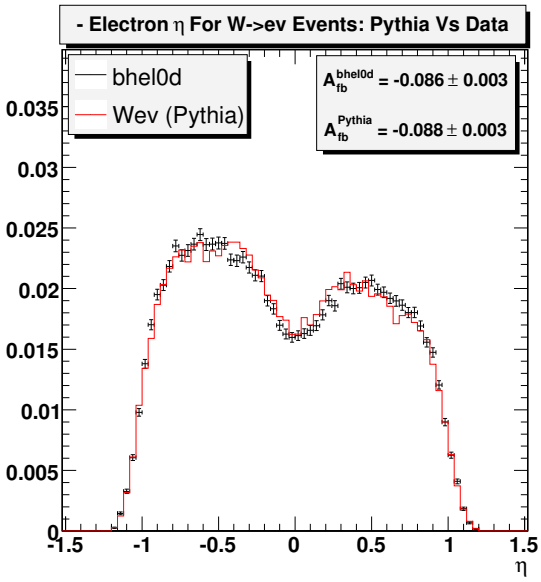

Figure 5.3: - Electron (CEM) η For W + 0 Jet Events

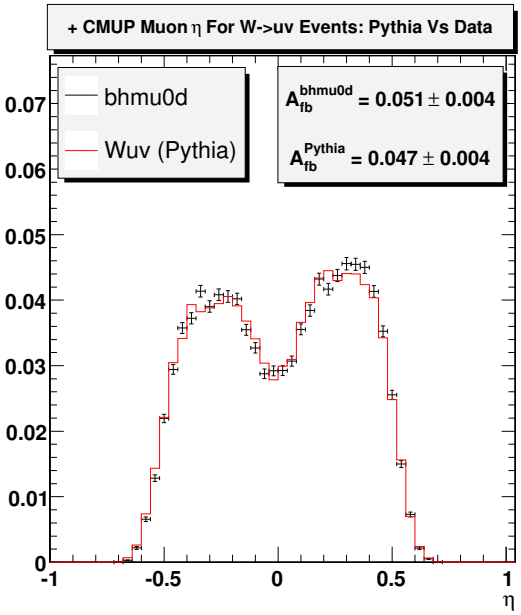

Figure 5.4: + Muon (CMUP) η For W + 0 Jet Events

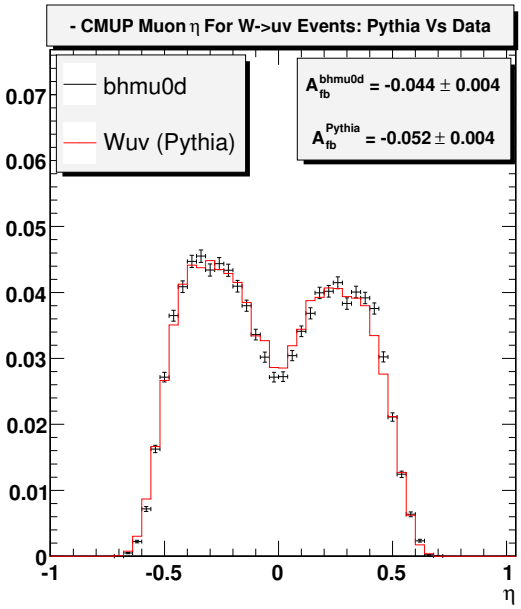

Figure 5.5: - Muon (CMUP) η For W + 0 Jet Events

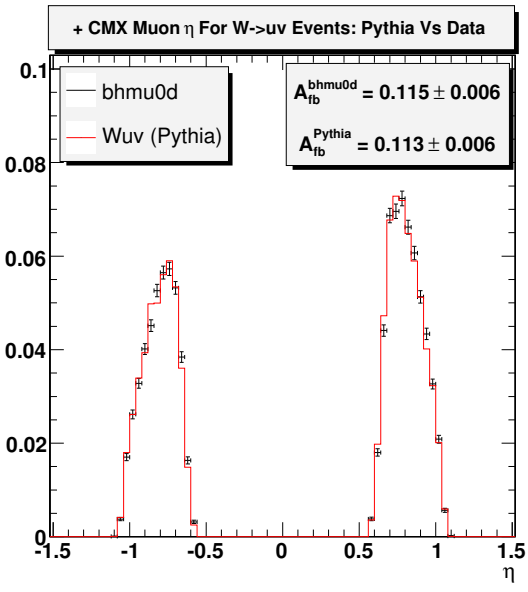

Figure 5.6: + Muon (CMX) η For W + 0 Jet Events

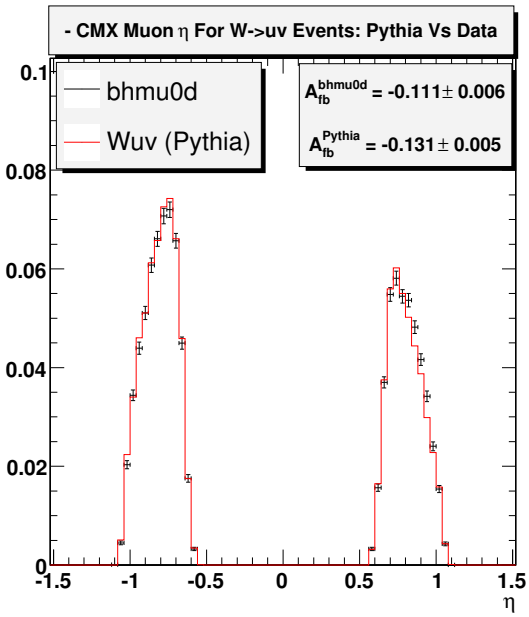

Figure 5.7: - Muon (CMX) η For W + 0 Jet Events

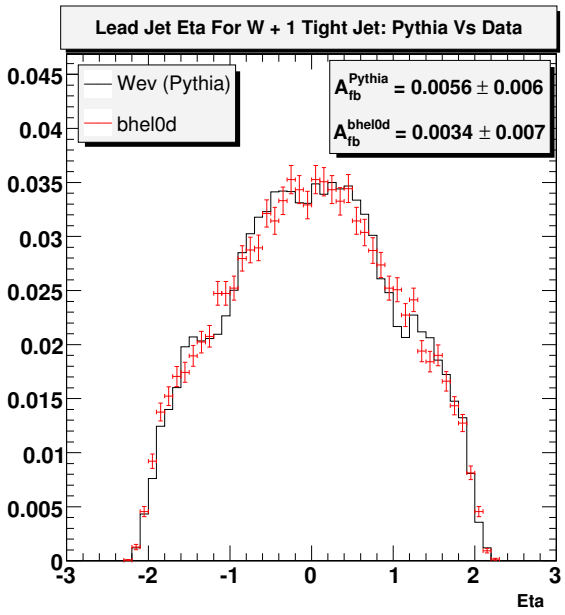

Figure 5.8: Leading Jet η For W + 1 Jet Events

CHAPTER 6

Calculation Of The Front-Back Asymmetry

6.1 $t\bar{t}$ Event Reconstruction

The measurement of A_{fb} will use the production angle of the top quark. The top quark is not directly observed in the detector, and therefore, we must reconstruct its momentum 4-vector from the final state particles: jets, charged leptons and neutrino. Unfortunately, we measure only the transverse component of the neutrino (in the $\not\!\!E_T$) and it is impossible to identify the parent quark of a jet based upon detector information. Because the type of parton cannot be identified by its jet, we cannot tell which jets came from which partons in a $t\bar{t}$ event. If we are to reconstruct the event we must find a method to choose the correct jet-parton assignments, as illustrated in Figures 6.1 and 6.2. We have developed an algorithm to match jets to the correct partons and reconstruct the full neutrino momentum by employing several constraints available in the "$t\bar{t}$ lepton plus jets hypothesis". This method allows us to reconstruct the complete kinematics of the $t\bar{t}$ final state.

6.1.1 Matching Jets To Quarks And Reconstructing The Neutrino

The problem of reconstrucing the $t\bar{t}$ event is a combinatoric one: we must choose between a number of possible arrangements. The highest four energy jets in the event are assumed to come from the four quarks in the $t\bar{t}$ process. Matching four jets to four

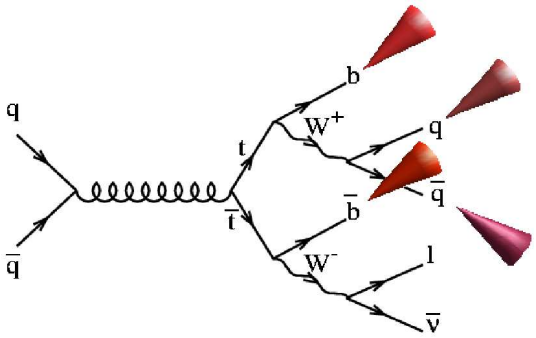

Figure 6.1: $t\bar{t}$ Lepton Plus Jets Event

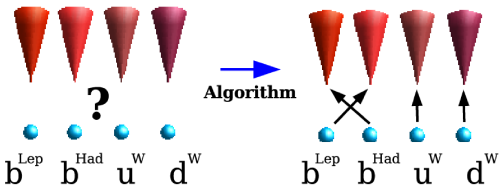

Figure 6.2: Matching Jets To Quarks

quarks leads to 24 possible combinations. This can be reduced by a factor of two since interchanging the two quarks from W-boson decay does not change the kinematics of the event.

Because we cannot measure the momentum of the event along the beam direction, we cannot infer the P_z of the neutrino from "missing E_z". However, we can calculate the neutrino P_z by requiring that the lepton and neutrino be consistent with the known mass of the W-boson. This calculation involves a quadratic equation and produces two solutions for the neutrino P_z. Both solutions are considered. Together with the jet assignments, the event has 24 possible combinations.

Our strategy is to test each combination for consistency with the "$t\bar{t}$ hypothesis". That hypothesis has four main components:

- The lepton and neutrino are decay products of a W-boson ($W \rightarrow l\nu$)
- Two jets are decay products of a W-boson ($W \rightarrow jj$)
- The lepton, neutrino, and a third jet are final states from a top quark decay ($t \rightarrow l\nu j$)
- The two jets from $W \rightarrow jj$ and a fourth jet are final states from the other top quark decay ($t \rightarrow jjj$)

The consistency of each combination with the $t\bar{t}$ hypothesis is assessed with a χ^2 test.

The χ^2 equation is:

$$\chi^2 = \sum_{i=l,jets} \frac{(p_t^{i,meas} - p_t^{i,fit})^2}{\sigma_i^2} + \sum_{j=x,y} \frac{(p_j^{UE,meas} - p_j^{UE,fit})^2}{\sigma_j^2} + \frac{(M_{jj} - M_W)^2}{\Gamma_W^2} + \frac{(M_{lv} - M_W)^2}{\Gamma_W^2} + \frac{(M_{bjj} - M_{fit})^2}{\Gamma_t^2} + \frac{(M_{blv} - M_{fit})^2}{\Gamma_t^2} \tag{6.1}$$

While we are assessing the "goodness-of-fit" we can also take the opportunity to make modest corrections to the jet energies. The last four terms are the constraints. M_{jj} is the invariant mass of the two jets that must be consistent with the known W boson mass. M_{bjj} and M_{lvb} are the invariant masses of the hadronically decaying and leptonically decaying top quark side. These should be consistent with being equal, and their common value, M_{fit} is the best estimate of the top quark mass. M_{lv} is the mass of the lepton and the neutrino which must be consistent with the mass of a W boson. All four of the constraints are particle masses, and their weights are the theoretical decay width of the particle.

The first two terms are sums over lepton and jet transverse energies and "unclustered" energy, which is the energy in the event outside the $t\bar{t}$ interaction. These values are varied within their measured error. This improves resolution on jet energies, as well as the probability of finding the correct combination. The known top quark mass may also be used as a further constraint in the fit by setting $M_{fit} = M_{known}$.

The standard package MINUIT is used to vary the independent parameters and minimize the χ^2 for each possible combination of jet-parton assignments and neutrino solutions [21]. The combination with the lowest χ^2 is chosen as the best representative of the $t\bar{t}$ hypothesis for the event. Tests with Monte Carlo simulations show that the correct assignment is chosen 45% of the time, and this improves to 60 % in the constrained fit. In this analysis, any event with a $\chi^2 > 50$ is removed from the sample. This eliminates events that are badly measured as well as some fraction of background events.

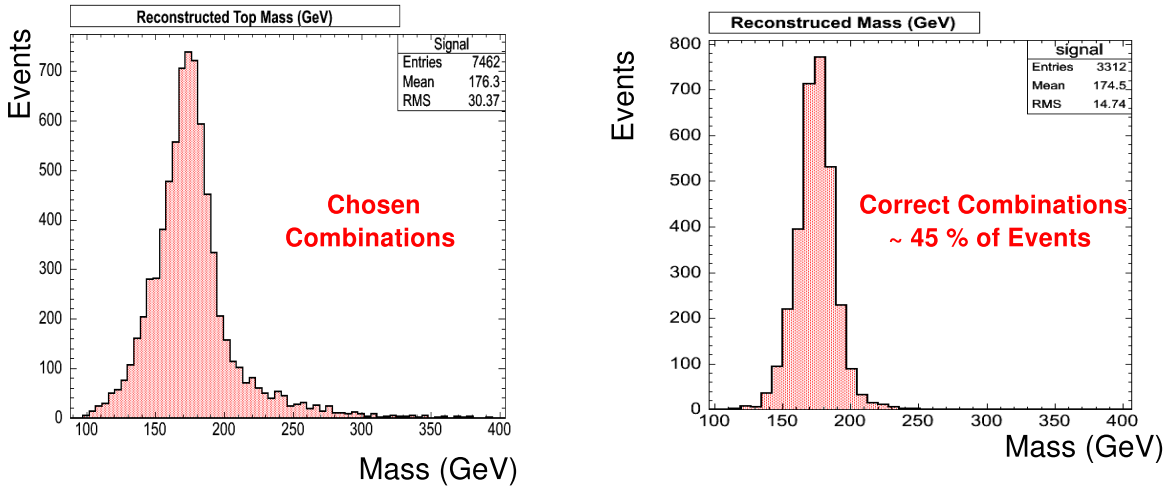

Figure 6.3: Reconstructed Mass For Chosen And Correct Combinations.

6.2 Reconstructed vs True Distributions

Figure 6.3 shows the reconstructed mass for the chosen and the correct jet-parton assignments in $t\bar{t}$ Monte Carlo with $M_t = 178$ GeV/c^2 and $\Gamma_t = 1.5$ GeV. Even for correct jet-parton assignments, the reconstructed distribution has a mean shifted from 178 GeV/c^2, and a smeared width much larger then 1.5 GeV. This is due to the measurement resolution of the energy of jets, leptons, and the missing energy. The chosen solution has events with both correct and incorrect jet-parton assignments. Incorrect jet-parton assignments further distort the mass distribution. These kinds of distortions will be an issue for any reconstructed distribution.

In order to draw conclusions about the "true" value of a quantity or measurement, the measured one will need to be corrected for these effects. The example shown here illustrates that the Monte Carlo simulation is a useful tool for this, as long as it is a faithful representation of reality. We discuss next how we use the Monte Carlo to assess the reconstruction and resolve some fundamental issues with our measurement.

6.3 Comparison Of Reconstructed Data To The Model

The algorithm has been applied to $t\bar{t}$ signal and background models as described in chapter 5, and 695 pb^{-1} of data collected at CDF. The signal and background models are normalized to the predicted values shown in Table 4.3 (53.6 background events and 203.4 signal events). We now compare a few example distributions in data and the model.

6.3.1 χ^2

The shape of the χ^2 distribution is a measure of the compatibility of events with the assumption that they originate from $t\bar{t}$ lepton plus jets processes. If the reconstruction of $t\bar{t}$ events is not well simulated by our model or normalization is incorrect, then the χ^2 distribution in data will diverge from predicted. The χ^2 distribution for data and our model is shown in Figure 6.4. The data and the model agree in shape and rate of decay far out into the tails. At the very outer edges of the tails ($\chi^2 > 50$) a few events in data appear. This is consistent with an integration of the number of events in the model predicted to have $\chi^2 > 50$. The good agreement between model and data is a high level check that event reconstruction of our model is an accurate simulation of event reconstruction in data.

6.3.2 Top Mass

The reconstruction algorithm has been used by the CDF collaboration to perform the most accurate measurement of the top mass to date, 173.4 $\pm$ 2.8 GeV/c^2 in 680 pb^{-1} [22]. The distribution of the reconstructed mass should be another good quality control indicator for our analysis. The distribution of the reconstructed mass returned by the algorithm is shown in Figure 6.5 for our model and data. The shape of the data at the low end of the spectrum follows the characteristic bump in the model which is due to

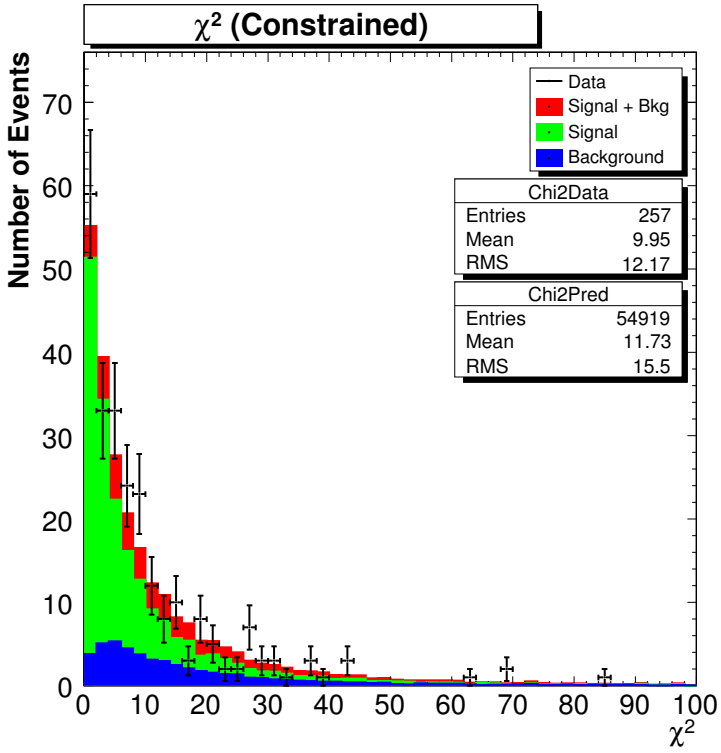

Figure 6.4: χ^2 Distribution

backgrounds. At the peak of the distribution, which contains the bulk of events, the model and data follow the same sharp rise and decline. Even far out into the tails of the distribution, where little background exist, both model and data have similar shape. The good agreement between Monte Carlo and data, shown in 6.5, again suggest that our models are an accurate reflection of the data.

6.3.3 Top Quark Kinematics

To study quantities other than the mass, we can impose an additional constraint in the reconstruction that the top mass be consistent with our measured value. The default for our mass constrained reconstruction is $M_t = 175$ GeV/c^2, which is consistent with out measurement of $M_t = 173.4 \pm 2.8$ GeV/c^2 [22]. As discussed in section 6.1.1, this increases the number of correct jet-parton assignments by 15%. In all analysis following,

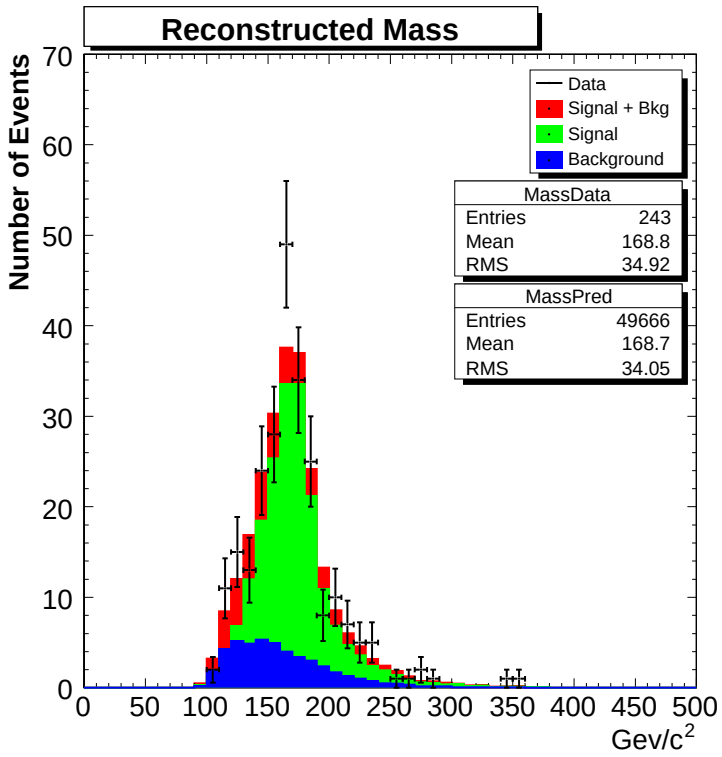

Figure 6.5: Reconstructed Top mass

this constraint is imposed.

The top quark transverse momentum is shown in Figure 6.6. The lack of events near $P_t = 0$ reflects the effect due to the kinematic cuts on jets, leptons, and missing energy in event selection: it is an acceptance effect. The data and our model are in good agreement over the entire spectrum.

The distribution of the invariant mass of the $t\bar{t}$ system is shown in Figure 6.7. No events are reconstructed with $M_{t\bar{t}} < 350$ due to the top mass constraint. The data and our model are consistent in the shape of the distribution from peak to tail: each show a slow exponential decline in number of events beginning at $M_{t\bar{t}} = 350$ with very few events with $M_{t\bar{t}} > 600$.

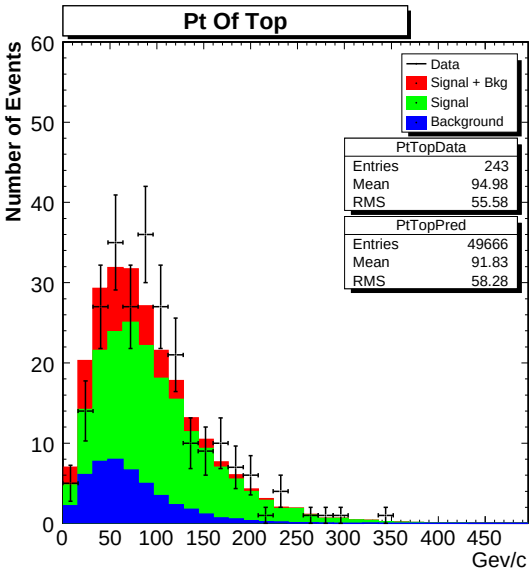

Figure 6.6: P_t Of Top

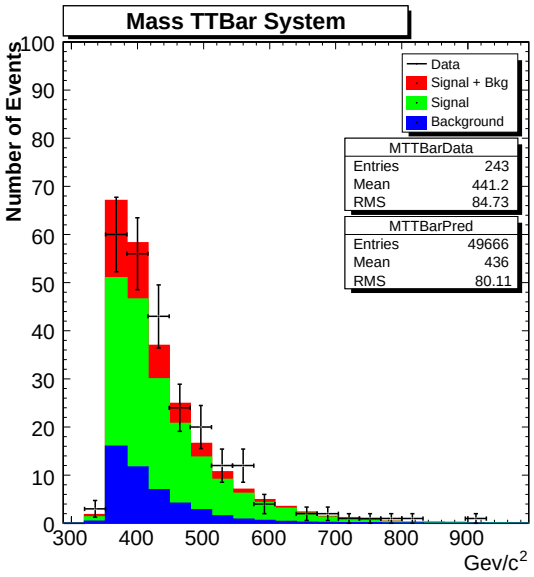

Figure 6.7: Invariant Mass $t\bar{t}$ System

6.3.4 Top Production Angle

The top production angle Θ, is the angle between the outgoing top quark and the initial proton direction:

$$\Theta = tan^{-1}\left(\frac{P_t}{P_z}\right) \tag{6.2}$$

The use of a polar angle is somewhat unconventional in hadron collider physics. The usual choice is to transform to a closely related quantity called the rapidity:

$$y = \frac{1}{2} \cdot ln\left(\frac{E + P_z}{E - P_z}\right) \tag{6.3}$$

For a massless particle, y is approximately equal to the pseudo-rapidity, defined in equation 2.2. These variables are generally convenient because they are invariant against Lorentz transformations along the beamline. However, in our measurement we find that

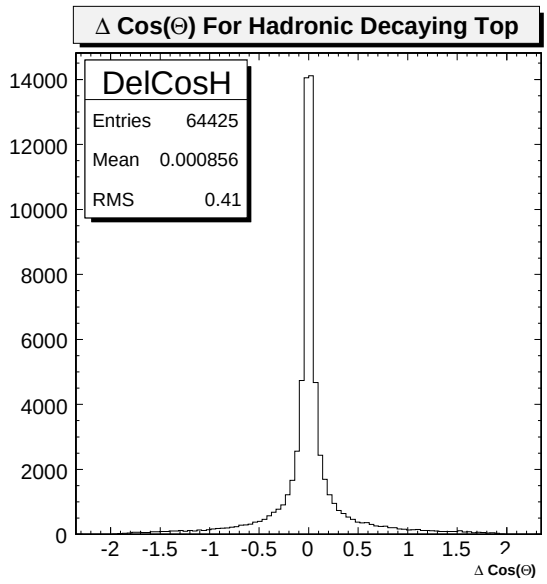

Figure 6.8: Resolution Of Cos(Θ), Hadronic Top Decay

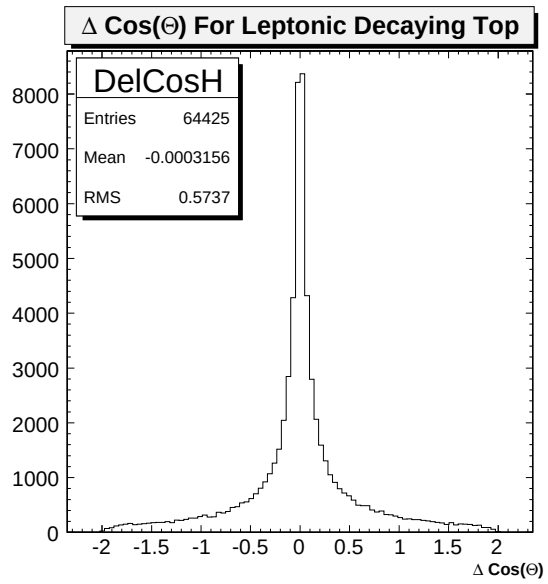

Figure 6.9: Resolution Of Cos(Θ), Leptonic Top Decay

the polar angle is most convenient in studies of reconstruction, and we will develop our A_{fb} formalism around it.

6.3.5 Issues In The Production Angle Reconstruction

Because $Cos(\Theta)$ is central to our analysis, we study its reconstruction in further detail. To assess the accuracy of the reconstruction we compare the "true" value of the angle in top simulation to the reconstructed one. Our figure of merit is the difference:

$$\Delta Cos(\Theta) = Cos(\Theta)_{True} - Cos(\Theta)_{Recon} \tag{6.4}$$

The distribution of $\Delta Cos(\Theta)$ is shown in Figure 6.8 for the hadronically decaying top quarks in our model of $t\bar{t}$. This histogram shows that the majority of events are in a narrow peak with $|\Delta Cos(\Theta)| \leq 0.1$. The histogram illustrate that the algorithm effectively reconstructs the production angle of the top quark.

If charge conjugation symmetry is assumed in the production mechanism, then the

production angle can be measured using either the hadronic or leptonic decaying top quark. $\Delta Cos(\Theta)$ for the leptonically decaying top quark is shown in Figure 6.9. The hadronically decaying top quark is more accurately reconstructed, with 1.4 times smaller RMS then leptonic decaying top quark. The reconstruction of the production angle of the leptonically decaying top quark is degraded by the lack of constraint in the longitudinal momentum. Because of this, we will use the hadronically decaying top quark to measure the production angle.

6.3.6 The Front-Back Asymmetry

Shown in Figure 6.10 is the production angle distribution for the hadronically decaying top quark, $(-Q_l) \cdot Cos(\Theta)$, where we have used the charge of the lepton, $-Q_l$, to infer the charge of the top quark. The forward backward asymmetry of this distribution is calculated by:

$$A_{fb} = \frac{N_{(-Q_l)\cdot Cos(\Theta)>0} - N_{(-Q_l)\cdot Cos(\Theta)<0}}{N_{(-Q_l)\cdot Cos(\Theta)>0} + N_{(-Q_l)\cdot Cos(\Theta)<0}} \tag{6.5}$$

The result in data and our model is:

$$A_{fb}^{data} = 0.095 \pm 0.063 \tag{6.6}$$

$$A_{fb}^{model} = 0.010 \pm 0.006 \tag{6.7}$$

The data shows a slight excess, which is nevertheless consistent with expectations within the large statistical error. In order to make a comparison to the theoretical prediction we must understand how to correct the reconstruction back to the "true" value. The corrections to the measurement are discussed in the next chapter.

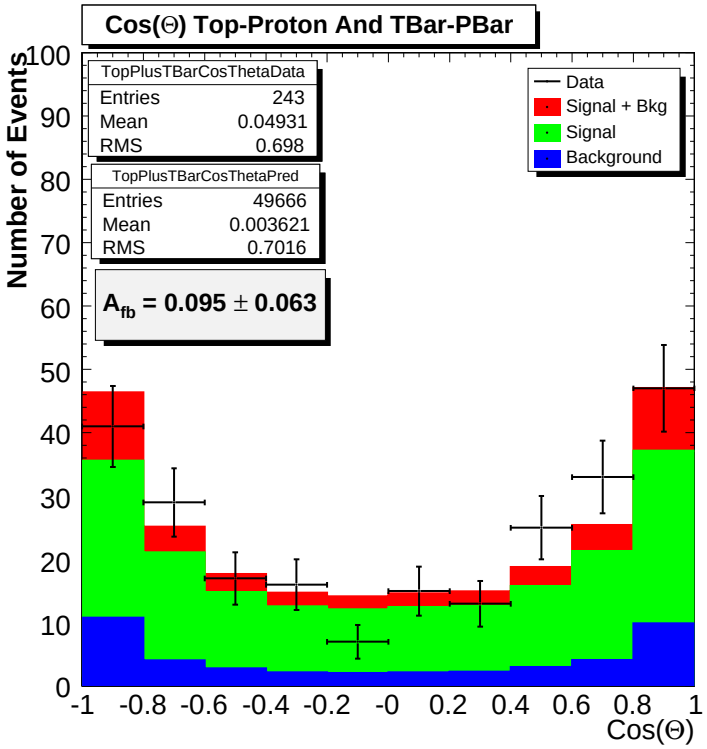

Figure 6.10: $(-Q_l) \cdot Cos(\Theta)$ Of Hadronic Decaying Top

CHAPTER 7

Corrections To The Measured A_{fb}

In order to compare the measured front-back asymmetry to the theoretical prediction, we must account for any bias and smear of the $t\bar{t}$ asymmetry due to backgrounds, acceptance, and reconstruction. Our Monte Carlo model is expected to simulate these effects, and we use these simulations to understand and develop corrections.

Each correction is tailored to events in six different categories based upon the the high P_t lepton trigger and the lepton charge. These categories are $\pm CEM$, $\pm CMUP$, and $\pm CMX$. This is done to provide specific corrections to events which are detected with similar apparatus and selected with similar criteria.

Each individual effect and the corresponding corrections are described in the following sections.

7.1 Background Corrections

In chapter 4 we described a number of backgrounds to the $t\bar{t}$ signal. All non-signal processes dilute the measurement. In addition, several of these backgrounds contain intrinsic asymmetries due to parity violating weak interactions, and these will bias the measurement.

Our remediation of this complication is a straight-forward subtraction. Each back-

ground model is run through reconstruction, giving an estimate of the ratio of forward to backward events. An absolute normalization is available from the background estimate described in chapter 4. We then subtract the predicted number of forward and backward background events from the number measured in data.

The reconstructed production angle, $(-Q_l) \cdot Cos(\Theta)$, for the combined background model is shown in Figure 7.1. The contributions from the different background processes are stacked on one another. Compared to the $t\bar{t}$ signal model in Figure 6.10, the production angle in backgrounds is distributed much closer to the p and $\bar{p}$ direction ($Cos(\Theta) = \pm 1$). Therefore, the signal to background ratio will be larger then average at the outer edges of this distribution.

The predicted A_{fb} and normalization for each individual background is shown in Tables 7.1 through 7.6. The combined background asymmetry in all lepton categories for the reconstructed production angle distribution, $(-Q_l) \cdot Cos(\Theta)$, is:

$$A_{fb}^{Total\ Bkg} = -0.013 \pm 0.012$$

which is consistent with zero. Therefore, the largest effect the background has on the measurement is to dilute the $t\bar{t}$ signal.

The estimated number of forward and backward background events needs to be corrected separately for each kind of lepton. The number and uncertainty in each category is:

$$F_{bkg} = \frac{N_{bkg}}{2} \cdot (1 + A_{fb,\,bkg}) \tag{7.1}$$

$$\sigma^2_{F_{bkg}} = \sum_{i=bkg} \sigma^2_{A^i_{fb}} \cdot \frac{N^j_{bkg}}{2} \tag{7.2}$$

$$B_{bkg} = \frac{N_{bkg}}{2} \cdot (1 - A_{fb,\,bkg}) \tag{7.3}$$

$$\sigma^2_{B_{bkg}} = \sum_{i=bkg} \sigma^2_{A^i_{fb}} \cdot \frac{N^j_{bkg}}{2} \tag{7.4}$$

where,

$N^i_{bkg} = \#$ events in i^{th} background

$N_{bkg} =$ Total # of events in lepton category

$A^i_{fb,\,bkg} = A_{fb}$ for i^{th} background

$A_{fb,\,bkg} = A_{fb}$ in lepton category

The error on background normalization will be considered as part of the systematic uncertainties in chapter 8. The measured number of forward and backward events is corrected for background contribution by subtracting the estimated contribution from the measurement.

$$F_{corr-bkg} = F_{meas} - F_{bkg} \tag{7.5}$$

$$\sigma^2_{F_{corr-bkg}} = \sigma^2_{F_{meas}} + \sigma^2_{F_{bkg}} \tag{7.6}$$

$$B_{corr-bkg} = B_{meas} - B_{bkg} \tag{7.7}$$

$$\sigma^2_{B_{corr-bkg}} = \sigma^2_{B_{meas}} + \sigma^2_{B_{bkg}} \tag{7.8}$$

where,

$F, B_{meas} =$ Measured # F,B events in data

$\sigma_{F,B_{meas}} =$ Error on F, B_{meas} (Poisson)

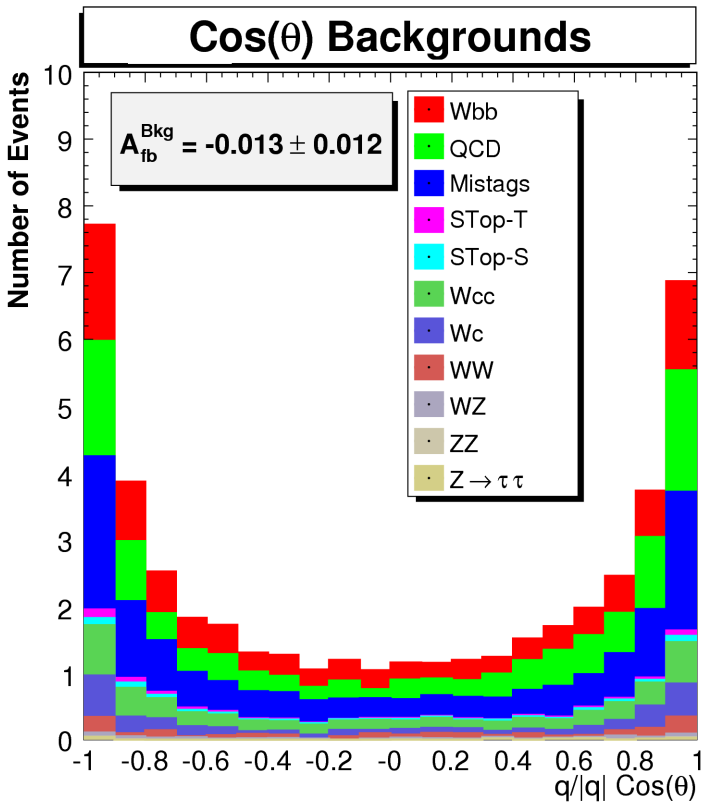

Figure 7.1: $\frac{q}{|q|} \cdot Cos(\Theta)$ For Backgrounds

The number of forward and backward events remaining after background subtraction is now treated as $t\bar{t}$ signal.

Table 7.1: A_{fb}^{Bkg} +CEM Electron Events

Background	A_{fb}	N_{Events}^{Model}
QCD	-0.07±0.08	3.4
W+LF Mistags	0.028±0.016	3.5
W$b\bar{b}$	0.082±0.02	3.0
W$c\bar{c}$	0.07±0.04	1.3
Wc	-0.24±0.3	0.3
SingleTop-S	0.11±0.06	0.2
SingleTop-T	0.20±0.07	0.15
WW	-0.23±0.19	0.4
WZ	-0.10±0.18	0.1
ZZ	-0.20±0.44	0.01
Z→ $\tau\tau$	0.5±0.43	0.05
Combined	-0.01±0.02	12.3

Table 7.2: A_{fb}^{Bkg} -CEM Electron Events

Background	-CEM A_{fb}	N_{Events}^{Model}
QCD	0.10±0.08	3.5
W+LF Mistags	-0.082±0.016	3.5
W$b\bar{b}$	-0.11±0.02	3.0
W$c\bar{c}$	-0.07±0.04	1.2
Wc	-0.14±0.15	0.2
SingleTop-S	-0.06±0.06	0.2
SingleTop-T	-0.33±0.07	0.2
WW	0.07±0.19	0.4
WZ	0.15±0.13	0.2
ZZ	-0.23±0.27	0.02
Z→ $\tau\tau$	nil [a]	0.03
Combined	-0.04±0.02	12.3

[a]not enough events in MC

Table 7.3: A_{fb}^{Bkg} +CMUP Muon Events

Background	A_{fb}	N_{Events}^{Model}
QCD	-0.25±0.12	1.4
W+LF Mistags	0.018±0.022	2.1
W$b\bar{b}$	0.06±0.03	1.5
W$c\bar{c}$	0.02±0.06	0.8
Wc	0.05±0.07	1.1
SingleTop-S	-0.07±0.08	0.1
SingleTop-T	0.23±0.1	0.1
WW	0.11±0.23	0.3
WZ	0.0±0.27	0.07
ZZ	-0.67±0.3	0.01
Z→ $\tau\tau$	nil [a]	0.03
Combined	0.03±0.03	7.6

[a]not enough events in MC

Table 7.4: A_{fb}^{Bkg} -CMUP Muon Events

Background	A_{fb}	N_{Events}^{Model}
QCD	0.27±0.12	1.4
W+LF Mistags	-0.03±0.02	2.2
W$b\bar{b}$	-0.10±0.03	1.5
W$c\bar{c}$	-0.09±0.05	0.9
Wc	-0.04±0.08	0.7
SingleTop-S	-0.17±0.06	0.1
SingleTop-T	-0.06±0.07	0.1
WW	0.0±0.25	0.3
WZ	-0.29±0.26	0.07
ZZ	0.2±0.44	0.01
Z→ $\tau\tau$	nil [a]	0.01
Combined	0.01±0.03	7.3

[a]not enough events in MC

Table 7.5: A_{fb}^{Bkg} +CMX Muon Events

Background	A_{fb}	N_{Events}^{Model}
QCD	-0.07 ± 0.18	0.7
W+LF Mistags	0.09 ± 0.03	1.0
W$b\bar{b}$	0.12 ± 0.05	0.6
W$c\bar{c}$	0.04 ± 0.08	0.4
Wc	-0.05 ± 0.09	0.5
SingleTop-S	0.0 ± 0.14	0.04
SingleTop-T	0.12 ± 0.14	0.05
WW	-0.27 ± 0.29	0.2
WZ	0.43 ± 0.34	0.03
ZZ	nil [a]	0.0
Z→ $\tau\tau$	nil [b]	0.0
Combined	-0.03±0.05	3.5

[a]not enough events in MC
[b]not enough events in MC

Table 7.6: A_{fb}^{Bkg} -CMX Muon Events

Background	A_{fb}	N_{Events}^{Model}
QCD	-0.29 ± 0.16	0.7
W+LF Mistags	-0.05 ± 0.03	1.0
W$b\bar{b}$	-0.03 ± 0.05	0.6
W$c\bar{c}$	-0.12 ± 0.08	0.4
Wc	-0.07 ± 0.12	0.5
SingleTop-S	0.0 ± 0.14	0.04
SingleTop-T	-0.18 ± 0.17	0.05
WW	0.33 ± 0.54	0.2
WZ	-0.14 ± 0.37	0.03
ZZ	0.0 ± 0.71	0.0
Z→ $\tau\tau$	nil [a]	0.0
Combined	-0.1±0.05	3.3

[a]not enough events in MC

7.2 Acceptance Corrections

The reconstruction of the top quark production angle requires almost every component of the detector: hadronic and electromagnetic calorimeters, muon chambers, tracking chambers, and silicon tracking. Front-back asymmetries in detection efficiencies or acceptance will translate into an apparent asymmetry in measurement, which we will need to correct.

We use $t\bar{t}$ model to study how selection and the detector effect the measured number of forward and backward events. We define the selection efficiencies as follows:

$$\epsilon_F = \frac{F_{sel}}{F_{gen}} \tag{7.9}$$

$$\epsilon_B = \frac{B_{sel}}{B_{gen}} \tag{7.10}$$

where,

$F, B_{sel} = \#$ F,B events selected in MC

$F, B_{gen} = \#$ F,B events generated from MC

Using these efficiencies, the number of forward and backward events selected for analysis can be related to those generated by the matrix multiplication:

$$\begin{bmatrix} F_{sel} \\ \\ B_{sel} \end{bmatrix} = M_A \cdot \begin{bmatrix} F_{gen} \\ \\ B_{gen} \end{bmatrix} \tag{7.11}$$

where,

$$M_A = \begin{bmatrix} \epsilon_f & 0 \\ \\ 0 & \epsilon_b \end{bmatrix}$$

Since different lepton types are detected in separate apparatus with different geometries we study ϵ_f and ϵ_b in each case. Using 2 million $t\bar{t}$ simulated events, six matrices are formed for each of the six lepton categories; ±CEM electron, ±CMUP Muon, and ±CMX Muon. The elements of M_A for each lepton category are shown in Table 7.7.

Table 7.7: Elements Of M_A

Event Type	ϵ_f	ϵ_b
+CEM	0.0116±0.0001	0.0114±0.0001
-CEM	0.0113±0.0001	0.0120±0.0001
+CMUP	0.0100±0.0001	0.0100±0.0001
-CMUP	0.0090±0.0001	0.0100±0.0001
+CMX	0.0116±0.0001	0.0114±0.0001
-CMX	0.0113±0.0001	0.0120±0.0001

Defined in this way, these efficiencies are actually very close to the overall acceptance efficiency of the lepton plus jets selection. The efficiencies are low magnitude because most of the generated Monte Carlo events are $t\bar{t}$ dilepton and all-hadronic events, which our selection criteria removes. Dilepton and all-hadronic events that do pass selection are considered part of our sample. All categories show a small differences between the forward and backward efficiencies except events with a +CMUP muon.

7.3 Reconstruction Corrections

Mismeasured jet energies, incorrect jet-quark assignments, and charge misidentification contribute to a smearing effect in the reconstructed production angle, which can translate into a change in the populations of events measured forward and backward. This is demonstrated in Figures 7.2 and 7.3 for Monte Carlo Top events with a +CEM electron. We see that the effect of reconstructing into the wrong hemisphere occurs for 12 to 13% of top quarks.

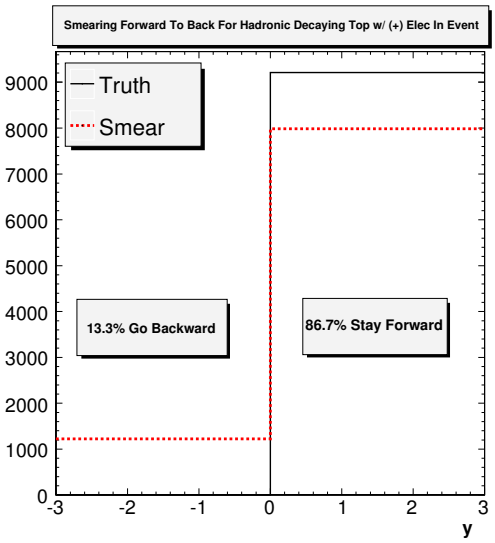

Figure 7.2: Demonstration Of Forward To Backward Smearing For +CEM Electron.

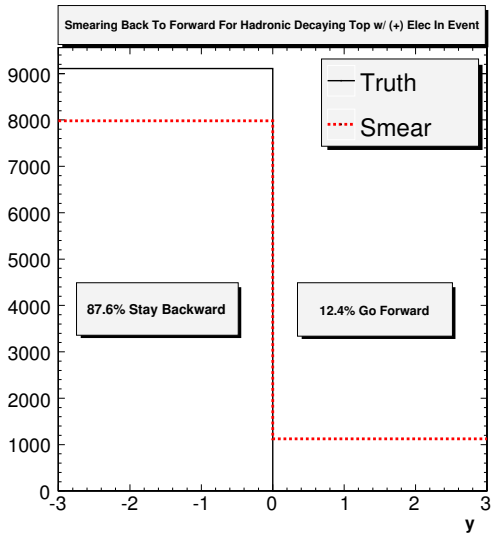

Figure 7.3: Demonstration Of Backward To Forward Smearing For +CEM Electron.

With this Monte Carlo based determination of smearing, we can correct out measurement using a further elaboration of our matrix formalism. We define a smearing matrix as follows. Let

$$\begin{bmatrix} F_{meas} \\ \\ B_{meas} \end{bmatrix} = M_R \cdot \begin{bmatrix} F_{sel} \\ \\ B_{sel} \end{bmatrix} \tag{7.12}$$

where,

$$M_R = \begin{bmatrix} \lambda_{ff} & \lambda_{bf} \\ \\ \lambda_{fb} & \lambda_{bb} \end{bmatrix}$$

The elements of M_R are defined as follows:

$$\begin{aligned} \lambda_{ff} &= \frac{F_{sel}(F)}{F_{sel}} \qquad & \lambda_{bf} &= \frac{F_{sel}(B)}{B_{sel}} \\ \lambda_{fb} &= \frac{B_{sel}(F)}{F_{sel}} \qquad & \lambda_{bb} &= \frac{B_{sel}(B)}{B_{sel}} \end{aligned} \tag{7.13}$$

where,

$$\begin{aligned} F_{sel} &= \#\text{ Forward events selected (as in eqn 7.9)} \\ B_{sel} &= \#\text{ Backward events selected (as in eqn 7.9)} \\ F_{sel}(F) &= \#\text{ Selected forward events reconstructed forward} \\ F_{sel}(B) &= \#\text{ Selected forward events reconstructed backward} \\ F_{sel}(F) &= \#\text{ Selected backward events reconstructed forward} \\ F_{sel}(F) &= \#\text{ Selected backward events reconstructed backward} \end{aligned}$$

Using our Monte Carlo model we can estimate the elements of M_R for each category of lepton. The errors are binomial because each event is reconstructed either forward or backward:

$$\sigma_{M_R} = N_{events} \cdot p \cdot (1 - p) \tag{7.14}$$

where p is λ_{ij}.

The off-diagonal element of Table 7.8 reproduce the conclusion from Figures 7.2 and 7.3.: between 13 and 15% of events are reconstructed in the wrong direction. The matrices also show a slight difference in the off-diagonal elements. This is because the reconstructed distribution in our Monte Carlo model is dependent on event selection. As seen in Table Table 7.7, event selection is slightly asymmetric. This skews the production angle distribution in the $t\bar{t}$ model, which propagates into the reconstructed distribution.

Table 7.8: Elements Of M_R

Event Type	λ_{ff}	λ_{bf}	λ_{fb}	λ_{bb}
+CEM	0.852±0.009	0.147±0.009	0.136±0.009	0.876±0.009
-CEM	0.867±0.009	0.134±0.009	0.144±0.009	0.856±0.009
+CMUP	0.848±0.010	0.152±0.010	0.143±0.010	0.857±0.010
-CMUP	0.869±0.010	0.131±0.010	0.147±0.010	0.852±0.010
+CMX	0.848±0.010	0.152±0.010	0.143±0.010	0.857±0.010
-CMX	0.869±0.010	0.131±0.010	0.147±0.010	0.852±0.010

7.4 Total Correction To The Measured A_{fb}

With the understanding of acceptance and reconstruction bias in hand, we can develop an overall formalism for correcting the measured A_{fb} back to the true A_{fb} of $t\bar{t}$ production. Matrices M_A and M_R are multiplied together to create a relationship between the background corrected number of forward and backward events and the true number of forward and backward events generated in Monte Carlo. We will call the corrected values that are comparable to the number of events generated: F_{corr} and B_{corr}.

$$\begin{bmatrix} F_{corr-bkg} \\ \\ B_{corr-bkg} \end{bmatrix} = M_R \cdot M_A \cdot \begin{bmatrix} F_{corr} \\ \\ B_{corr} \end{bmatrix} \tag{7.15}$$

The combined matrix formed by multiplication of M_A and M_R is then inverted so that we can solve for the corrected values.

$$\begin{bmatrix} F_{corr} \\ \\ B_{corr} \end{bmatrix} = [M_R \cdot M_A]^{-1} \cdot \begin{bmatrix} F_{corr-bkg} \\ \\ B_{corr-bkg} \end{bmatrix} \tag{7.16}$$

We define the correction matrix M_C, where:

$$M_C = [M_R \cdot M_A]^{-1} = \begin{bmatrix} M_0 & M_1 \\ M_2 & M_3 \end{bmatrix} \tag{7.17}$$

Using the values from Tables 7.7 and 7.9, the elements of the correction matrix are calculated, shown in Table 7.9.

Table 7.9: Elements Of M_C

Event Type	M_0	M_1	M_2	M_3
+CEM	110.1	-18.0	-16.5	110.4
-CEM	111.9	-15.8	-17.6	106.3
+CMUP	171	-29.6	-27.4	173.2
-CMUP	177.4	-25.9	-29.4	170.8
+CMX	496.9	-99.9	-84.5	528.4
-CMX	513.1	-71.5	-82.6	500.9

We apply our correction matrices to the background corrected values from equations 7.7 and 7.5 . The corrected number of forward and backward events and their uncertainty is:

$$F_{corr} = F_{corr-bkg} \cdot M_0 + B_{corr-bkg} \cdot M_1 \tag{7.18}$$

$$\sigma^2_{F_{corr}} = \sigma^2_{F_{corr-bkg}} \cdot M_0^2 + \sigma^2_{B_{corr-bkg}} \cdot M_1^2 \tag{7.19}$$

$$B_{corr} = F_{corr-bkg} \cdot M_2 + B_{corr-bkg} \cdot M_3 \tag{7.20}$$

$$\sigma^2_{B_{corr}} = \sigma^2_{F_{corr-bkg}} \cdot M_2^2 + \sigma^2_{B_{corr-bkg}} \cdot M_3^2 \tag{7.21}$$

These values are used to calculate the final corrected asymmetry that may be compared to theoretical prediction.

$$A_{fb}^{corr} = \frac{F_{corr} - B_{corr}}{F_{corr} + B_{corr}} \tag{7.22}$$

$$\begin{aligned}\sigma^2_{A^{corr}_{fb}} = \; & \sigma^2_{F_{corr}} \cdot \left(\frac{2B_{corr}}{F_{corr}+B_{corr}}\right)^2 + \sigma^2_{B_{corr}} \cdot \left(\frac{2F_{corr}}{F_{corr}+B_{corr}}\right)^2 \\ & + \; 8 \cdot |F_{corr} \cdot B_{corr}| \cdot |M_0 \cdot M_2| \cdot \sigma^2_{F_{corr-bkg}} \\ & + \; \frac{|M_1 \cdot M_3|}{F_{corr}+B_{corr}} \cdot \sigma^2_{B_{corr-bkg}}\end{aligned} \tag{7.23}$$

7.4.1 Validation Of The Correction Procedure

Does this procedure really correct a measured asymmetry back to the true value? We will verify this by constructing Monte Carlo simulated samples with known asymmetries, applying our procedure, and comparing the results with the inputs.

Simulated A_{fb}

Our MC@NLO simulation has a real asymmetry which is probably too small to measure with our current dataset. To test realistic values, we need the statistics and flexibility of our Herwig model. It has no intrinsic asymmetry, but samples with asymmetry can be created by reweighting the production angle distribution of the top quark at the parton level.

The $Cos(\Theta)$ distribution from generic Herwig is shown in Figure 7.4. Let x represent the production angle, $f(x)$ is a 9th order polynomial fit to the distribution in Figure 7.4, and $a(x)$ is the asymmetric function we wish to add to $f(x)$ to produce our simulated asymmetric distribution. To produce the "new" distribution, $f(x)+a(x)$, we can reweight each event in the generic Herwig distribution by the value calculated in equation 7.24.

$$\text{New Weight is:} \quad \frac{\mathrm{f(x) + a(x)}}{\mathrm{f(x)}} \tag{7.24}$$

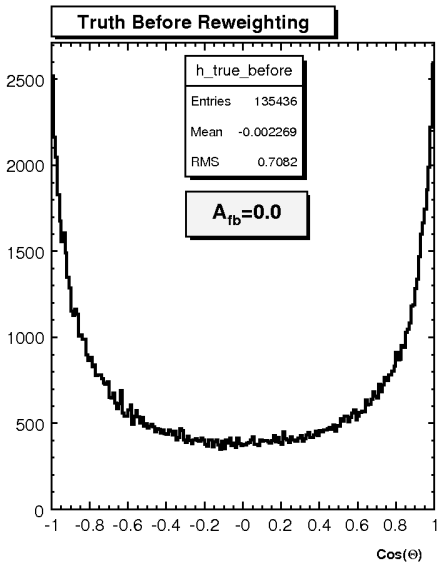

Figure 7.4: True $Cos(\Theta)$ Before Reweighting To 10%

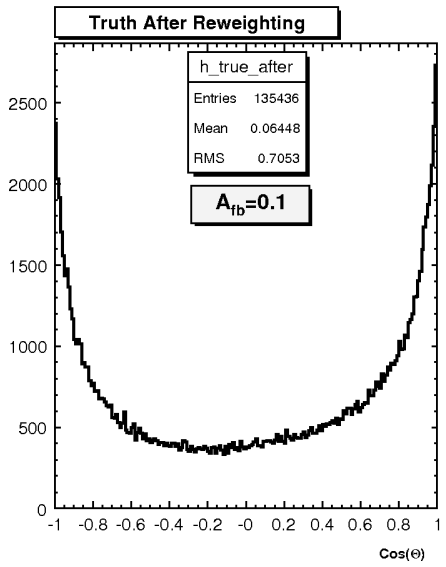

Figure 7.5: True $Cos(\Theta)$ After Reweighting To 10%

$$
\begin{aligned}
x &= Cos(\Theta) \\
f(x) &= \textstyle\sum_{i=0}^{9} \alpha_i \cdot x^i \text{ (Polynomial fit to original symmetric distribution)} \\
a(x) &= A_{fb} \cdot x
\end{aligned}
$$

This produces a $t\bar{t}$ production angle distribution which adds an asymmetry of magnitude A_{fb} to the symmetric form of the original.

As an example, the production angle distribution for events with a +CEM electron are reweighted to produce a 10% asymmetry. These events are then passed through event selection and reconstruction. The true and reconstructed distribution, before reweighting, are shown in Figures 7.4 and 7.6, and the reweighted distributions are shown in Figures 7.5 and 7.7. The reweighted true distribution has a linear increase from $Cos(\Theta) = -1$ to $Cos(\Theta) = 1$ and a 10% asymmetry. Both original and reweighted reconstructed distributions show the effects of smearing. The high peaks at the edges of both distributions, near $Cos(\Theta) = \pm 1$, are eroded into the center, and the reweighted distribution has a diluted asymmetry of 7.6%. The matrix M_R will be used to correct for these effects.

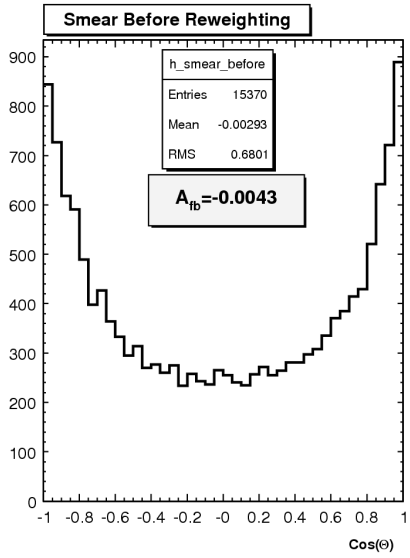

Figure 7.6: Reconstructed $Cos(\Theta)$ Before Reweighting To 10%

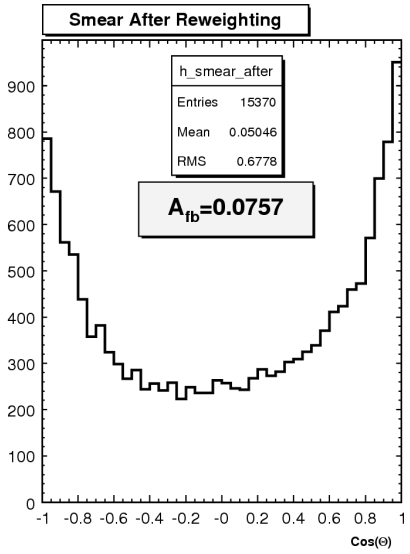

Figure 7.7: Reconstructed $Cos(\Theta)$ After Reweighting To 10%

Correcting Simulated A_{fb}

This technique is applied to produce a range of asymmetries between ±0.40. The A_{fb} is measured in each sample and then corrected using the matrices derived in section 7.4.

The results of our test are shown in Tables 7.11, 7.12, and 7.13 for ±CEM,±CMUP,and ±CMX categories. The combined result is shown in Table 7.10. The errors in the tables are entirely statistical. We conclude that, to first order, our correction procedure takes the measured A_{fb} back to the "true" values. A small over correction which increases with the size of A_{fb} may be evident but, the effect is small and will be treated as a systematic error for our measurement.

Table 7.10: Combined Bias Check

Input A_{fb}	Combined Measured A_{fb}
-0.4	-0.428±0.006
-0.2	-0.212±0.006
-0.1	-0.104±0.006
-0.05	-0.051±0.006
0.0	0.003±0.006
0.05	0.057±0.006
0.1	0.11±0.006
0.2	0.221±0.006
0.4	0.436±0.006

Table 7.11: Bias Check For CEM Case

Input A_{fb}	A_{fb}^{meas} +CEM	A_{fb}^{meas} -CEM
-0.4	-0.431±0.011	-0.414±0.012
-0.2	-0.215±0.012	-0.199±0.012
-0.1	-0.106±0.012	-0.094±0.012
-0.05	-0.053±0.012	-0.041±0.012
0.0	0.002±0.012	0.012±0.012
0.05	0.057±0.012	0.065± 0.012
0.1	0.109±0.012	0.118 ± 0.012
0.2	0.217±0.012	0.228±0.011
0.4	0.431±0.011	0.439±0.011

Table 7.12: Bias Check For CMUP Case

Input A_{fb}	A_{fb}^{meas} +CMUP	A_{fb}^{meas} -CMUP
-0.4	-0.431±0.015	-0.40±0.015
-0.2	-0.21±0.015	-0.19±0.015
-0.1	-0.102±0.015	-0.090±0.015
-0.05	-0.047±0.015	-0.037±0.015
0.0	0.007±0.015	0.015±0.015
0.05	0.062±0.015	0.067±0.015
0.1	0.117±0.015	0.12±0.015
0.2	0.230±0.015	0.231±0.015
0.4	0.447±0.015	0.439±0.015

Table 7.13: Bias Check For CMX Case

Input A_{fb}	A_{fb}^{meas} +CMX	A_{fb}^{meas} -CMX
-0.4	-0.486±0.024	-0.478±0.022
-0.2	-0.259±0.025	-0.256±0.023
-0.1	-0.14±0.03	-0.15±0.23
-0.05	-0.088±0.03	-0.1±0.02
0.0	-0.03±0.03	-0.04±0.02
0.05	0.032±0.03	0.013± 0.02
0.1	0.09±0.03	0.07±0.02
0.2	0.205±0.026	0.182±0.023
0.4	0.437±0.025	0.406±0.022

CHAPTER 8

Systematic Uncertainties

A number of complicating effects contribute to our measurement uncertainty in a way that is not yet reflected in our calculation. These additional "systematic" uncertainties will account for the possible imprecision in several important inputs to our model. Each uncertainty is treated in its own way, but the common technique is to compare our baseline model with one where one of the inputs has been varied within its known error.

8.1 Jet Energy Scale

Several corrections are applied to the measured energy of jets inside the detector. These corrections account for the response of calorimeters to different particles, non-linear response of the calorimeters to particle energies, regions of the detector without instrumentation, and energy radiated outside the jet clustering algorithm. Error associated with the determination of these corrections is assigned as a systematic error to the analysis. Each individual uncertainty in the jet energy scale is listed below.

- Relative Correction

  Corrections due to η dependent calorimeter response.

- Underlying Event Correction

  Correcting for energy associated with the spectator partons in the event.

- Absolute Correction

  Corrects the jet energy measured in the calorimeter for any non-linearity and energy loss in the un-instrumented regions of each calorimeter.

- Out Of Cone Correction

  Corrects back to particle-level energy by accounting for leakage of radiation outside the jet clustering cone.

- Splash Out Correction

  Uncertainty in the energy leakage beyond the out of cone scope.

The uncertainty due to the jet energy scale could cause different portions of the detector to over or under correct the amount of energy in jets, and therefore create a bias in the measurement of the asymmetry. For example, if the forward region of the detector was overcorrected compared to the backward region this would cause an asymmetry in the measurement. If there is a bias in the jet energy scale as a function of η, the shape of the production angle distribution predicted by Monte Carlo could be distorted. The Monte Carlo may not correctly model the "real" complexities of the jet-parton assignment. The error in the jet energy scale would also be responsible for error in the correction matrices defined in Section 7.

The combined uncertainty of the jet energy scale is the quadrature sum of the individual uncertainties. A "shifted" sample is created by applying a scale factor to the energy of individual jets that represents a 1.0σ uncertainty in the jet energy scale. Two such samples are created: a $+1.0\sigma$ sample and a -1.0σ sample. The "jet energy shifted" samples and our default model are reweighted to have an asymmetry of 0.1. We then apply our measurement procedure to these samples and calculate the difference between the two shifted samples, and then calculate the difference between each shifted sample

and the default sample. The largest value is taken as the systematic uncertainty.

Table 8.1: Jet Energy Scale Error

Event Type	$+\Delta$	$-\Delta$	Diff/2	$\|Max\|$
+CEM	-0.006	0.002	0.002	0.006
-CEM	-0.001	-0.005	-0.003	0.005
+CMUP	0.003	0.002	0.003	0.003
-CMUP	-0.003	0.006	0.002	0.006
+CMX	0.01	-0.015	-0.003	0.015
-CMX	-0.004	-0.001	-0.003	0.004
Combined				0.006

8.2 Background Shape

The shape of the production angle for each background component can be unique. Fluctuations in the relative contributions of each background will distort the overall shape of the background production angle, change the background asymmetry, and lead to an error in the background correction. We estimate the systematic uncertainty due to this effect by the technique of "pseudo-experiments".

Each "pseudo-experiment" contains approximately the number of signal and background events expected in our data sample. These events are drawn from our "models", as described in chapter 5, in an amount that represents Poisson fluctuations around the expected mean of each type. We pass these events through our full measurement procedure and record the resulting measured A_{fb}. If our procedure is correct, the resulting "spectrum" of A_{fb} from many pseudo-experiments should have a mean that represents the underlying true $t\bar{t}$ A_{fb} and a width that represents the statistical error on the measurement.

We perform this procedure with reweighted signal events ($A_{fb} = 0.1$) and events from the background models described in chapter 5. We produce three $+1.0\sigma$ shifted samples and three -1.0σ shifted samples by changing the normalization of the three largest back-

grounds (QCD, $Wb\bar{b}$, W+LF) by a factor of 2 and 1/2. For each background, the largest difference between the default model and the shifted sample is taken as the systematic uncertainty. The combined systematic uncertainty for each lepton category is the quadrature sum of the uncertainties for each background. The result of this procedure is shown in Table 8.2.

Table 8.2: Background Shape

Event Type	$+\Delta_{QCD}$	$-\Delta_{QCD}$	$+\Delta_{W+HF}$	$-\Delta_{W+HF}$	$+\Delta_{W+LF}$	$-\Delta_{W+LF}$	$\sum_{quad}$
+CEM	-0.016	0.004	0.002	0.0	-0.002	0.0	0.016
-CEM	0.009	0.003	-0.016	0.012	-0.014	0.01	0.023
+CMUP	-0.02	0.01	-0.003	-0.001	0.003	0.005	0.021
-CMUP	0.006	-0.012	-0.02	-0.002	-0.02	0.0	0.031
+CMX	-0.017	0.001	-0.002	0.01	-0.008	0.004	0.019
-CMX	-0.019	0.032	0.0	0.01	0.01	0.012	0.036
Combined							0.022

8.3 Initial State Radiation (ISR)

Initial state radiation in $t\bar{t}$ events consists of gluons that are radiated from the production particles before hard collision. If the radiated gluons are energetic enough they will produce a jet that can be misidentified as one of the partons from the $t\bar{t}$ decay. The physics of this process in $t\bar{t}$ events is not yet well measured or understood, which leads to an uncertainty in the amount of ISR affecting our measurement procedure.

To calculate the systematic error due to uncertainty in ISR, we generate two $t\bar{t}$ simulated samples where the amount of ISR is shifted by $+1.0\sigma$ and -1.0σ of the theoretical error. The shifted ISR samples are reweighted to have an asymmetry of 0.1 and compared to our default $t\bar{t}$ Monte Carlo sample, also reweighted with an asymmetry of 0.1. We calculate the difference between the two shifted samples, and calculate the difference between each shifted sample and the default sample. The largest value is taken as the

systematic uncertainty.

Table 8.3: ISR Error

Event Type	$+\Delta$	$-\Delta$	Diff/2	$\lvert Max\rvert$
+CEM	-0.01	0.026	0.08	0.026
-CEM	0.004	0.008	0.006	0.008
+CMUP	0.008	-0.003	0.006	0.008
-CMUP	-0.015	-0.006	0.005	0.006
+CMX	-0.014	-0.015	0.0	0.0015
-CMX	-0.065	-0.018	0.018	0.065
Combined				0.017

8.4 Final State Radiation (FSR)

Final state radiation in $t\bar{t}$ events consists of gluons that are radiated from the final state particles. If the radiated gluons are energetic enough they will produce a separate jet. FSR produces measurement error because it creates two jets both from the same parton but with less energy. One of these jets can be used in reconstruction with mismeasured energy or both could enter reconstruction which would displace the "correct" jet from the reconstruction process. The physics of this process in $t\bar{t}$ events is not yet well measured, which leads to an uncertainty in the amount of FSR affecting our measurement procedure.

To calculate the systematic error due to uncertainty in FSR, we generate two $t\bar{t}$ simulated samples where the amount of FSR is shifted by $+1.0\sigma$ and -1.0σ of the theoretical error. The shifted FSR samples are reweighted to have an asymmetry of 0.1 and compared to our default $t\bar{t}$ Monte Carlo sample, also reweighted with an asymmetry of 0.1. We calculate the difference between the two shifted samples, and calculate the difference between each shifted sample and the default sample. The largest value is taken as the systematic uncertainty.

Table 8.4: FSR Error

Event Type	$+\Delta$	$-\Delta$	Diff/2	$\|Max\|$
+CEM	-0.001	-0.023	-0.012	0.023
-CEM	0.01	-0.01	0.001	0.01
+CMUP	0.042	0.028	0.04	0.042
-CMUP	-0.01	0.01	0	0.01
+CMX	-0.023	0.019	-0.002	0.023
-CMX	0.008	0.0	0.004	0.008
Combined				0.019

8.5 Mass Of The Top Quark

As described in chapter 6, the known mass of the top quark is used as a constraint in reconstruction. If the mass of the top quark is different from our constraint, the reconstruction is fitting the data to the wrong hypothesis.

Two Monte Carlo simulations of $t\bar{t}$ events, one with mass 175 GeV and the other with 178 GeV, are reweighted to produce $A_{fb} = 0.10$. The samples are passed through our measurement procedure, except background subtraction, and the difference is considered the systematic error. The result is shown in Table 8.5.

Table 8.5: Mass Error

Event Type	Difference
+CEM	0.009
-CEM	0.001
+CMUP	-0.004
-CMUP	0.026
+CMX	-0.001
-CMX	-0.026
Combined	0.009

8.6 Monte Carlo Generator

Monte Carlo is expected to model the $t\bar{t}$ process from production to final state particles. This requires a number of effects to be simulated properly, such as top quark production,

top quark decay, and hadronization. Uncertainty in any number of these effects translates into uncertainty in our measurement. Fortunately, these simulations have been tested and refined over many measurements of many different processes. Nonetheless, we assign an uncertainty to our measurement to account for differences between our model and the actual $t\bar{t}$ process. We calculate the systematic error by comparing our measurement for two entirely different Monte Carlo simulations: Pythia and Herwig. Events from these two simulations are reweighted to produce an asymmetry of 0.1. The reweighted events are passed through our measurement procedure and the difference between the two measured values is taken as the systematic error. The result is shown in Table 8.6.

Table 8.6: MC Gen Error

Event Type	Difference
+CEM	-0.015
-CEM	0.001
+CMUP	-0.008
-CMUP	0.041
+CMX	-0.005
-CMX	-0.07
Combined	0.016

8.7 Parton Distribution Function (PDF)

The momentum distribution of partons and gluons in Monte Carlo simulations is derived from empirically calculated functions, called "PDF's". The momentum distribution of the particles in the hard scattering process determines the "energy" spectrum of the $t\bar{t}$ system. To study the effect on our measurement to the uncertainty in the PDF, we compare three different $t\bar{t}$ Monte Carlo samples generated with different PDF (CTEQ5L, MRST72, MRST75 [31] [32]) and reweighted to have an asymmetry equal to 0.1. The measurement procedure is applied to these three samples and the largest deviation of the measured value between any two samples is taken as the systematic uncertainty. The

result is shown in Table 8.7.

Table 8.7: PDF Error

Event Type	CTEQ5L-MRST72	CTEQ5L-MRST75	MRST72-MRST74	$\|Max\|$
+CEM	-0.009	-0.009	0.0	0.009
-CEM	0.014	-0.007	0.011	0.014
+CMUP	0.021	0.008	-0.013	0.021
-CMUP	0.003	0.02	0.012	0.02
+CMX	-0.009	-0.009	0.0	0.009
-CMX	0.06	0.046	-0.014	0.06
Combined				0.015

8.8 Correcting A_{fb}

In testing our correction procedure in section 7.4.1, we observed a slight over-correction in the measurement of A_{fb} that increased as a function of the input A_{fb}. The effect is small, but is treated as a systematic error in the analysis. The difference between the input A_{fb} and the corrected A_{fb} at an asymmetry equal to 0.2 is taken as the systematic uncertainty.

Table 8.8: Correcting A_{fb}

Event Type	Difference
+CEM	-0.017
-CEM	0.001
+CMUP	-0.03
-CMUP	0.01
+CMX	-0.005
-CMX	-0.06
Combined	0.02

8.9 Combined Systematic Uncertainty

The combined systematic uncertainty on the measurement of A_{fb} is calculated by adding each individual uncertainty in quadrature. The result is:

$$\sigma_{syst} = \pm 0.047 \tag{8.1}$$

CHAPTER 9

Measurement

We now carry out the full method described in this thesis to measure the forward-backward asymmetry for 695 pb^{-1} of data collected at CDF. Candidate $t\bar{t}$ lepton plus jets events are selected in data from the high Pt lepton triggers, as described in 3. The top production angle for each event is reconstructed using the algorithm described in 6, and the number of forward ($Cos(\Theta) > 0$) and backward ($Cos(\Theta) < 0$) events are counted. The predicted background contributions in the forward and backward hemispheres are subtracted. Bias and smearing are corrected with the procedure described in chapter 7. The front-back asymmetry is calculated from the corrected forward and backward counts by:

$$A_{fb} = \frac{N_{Forward} - N_{Backward}}{N_{Forward} + N_{Backward}} \tag{9.1}$$

This procedure is performed separately for events with $\pm CEM$ electrons, $\pm CMUP$ muons, and $\pm CMX$ muons. The asymmetries in each of these six categories are combined in a weighted average:

$$A_{fb} = \sum_{i=1}^{6} (-Q_l) \cdot A_{fb}^{i} \cdot \frac{N_{events}^{i}}{N_{events}^{Total}} \tag{9.2}$$

where i = $\pm CEM$, $\pm CMUP$, $\pm CMX$.

The step-by-step details of this procedure for 695 pb^{-1} of data collected at CDF are now described.

9.1 Event Selection

For the 695 pb^{-1} of data collected at CDF, 257 events are selected. The breakdown of those events into the type and charge of tight lepton found in the event is shown in Table 9.1. The data sample contains 154 events with a CEM electron, 72 with a CMUP muon, and 31 with a CMX muon. The number of positive to negative lepton events is almost equal, 126 to 131, as expected by charge conjugation symmetry, and the equality holds for all three lepton categories.

Table 9.1: Number Of Events By Lepton Category

Lepton Type	N_{Events}	% Of Total	N_{Events}^{Bkg}	Pred S/B
+CEM	77	30.0	12.43	6.2
-CEM	77	30.0	12.34	6.2
+CMUP	33	12.8	7.58	4.4
-CMUP	39	15.2	7.30	5.34
+CMX	16	6.2	3.50	4.6
-CMX	15	5.8	3.32	4.5

9.2 Reconstruction

The reconstruction algorithm is applied to events accepted from selection. A χ^2 cut at 50 is applied to remove poorly measured events. After the cut, 243 events remain from the original 257. The breakdown of these events among the six lepton categories is shown in Table 9.2.

The number of events in each category is reduced slightly or not at all by the χ^2 cut, and the relative contributions of each lepton category to the total number of events remain

Table 9.2: Event Counts After χ^2 Cut

Lepton Type	N_{Events}	Cut Efficiency (%)	% Of Total
+CEM	72	93.5	29.6
-CEM	74	96.1	30.4
+CMUP	32	97.0	13.2
-CMUP	35	89.7	14.4
+CMX	16	100.0	6.6
-CMX	14	93.3	5.8

almost the same.

The reconstructed production angle distributions for all categories are shown in Figures 9.1 to 9.6 along with the predicted distribution for signal and backgrounds. The combined distribution, $(-Q_l) \cdot Cos(\Theta)$, is shown in Figure 9.7. The shape of the production angle for each individual category and the combined data are in reasonable agreement withthe model prediction. The front-back asymmetry in each of these distributions is shown in Table 9.3.

Table 9.3: A_{fb} After Reconstruction

Lepton Type	N_{Events}^{Recon} F-B	A_{fb}^{Recon}
+CEM	39-22	0.08±0.12
-CEM	42-32	0.14±0.12
+CMUP	10-22	-0.38±0.16
-CMUP	20-15	0.14±0.17
+CMX	9-7	0.13±0.25
-CMX	9-5	0.29±0.26

As we showed previously in section 6.3.6, the combined asymmetry is:

$$A_{fb}^{recon} = 0.095 \pm 0.063 \tag{9.3}$$

Recall from chapter 6 that the raw predicted value from the model is 0.010±0.006.

Looking at the separate lepton categories, we see that the non-zero value of the asymmetry is mostly due to a large asymmetry in events with a CMUP muon. For events with

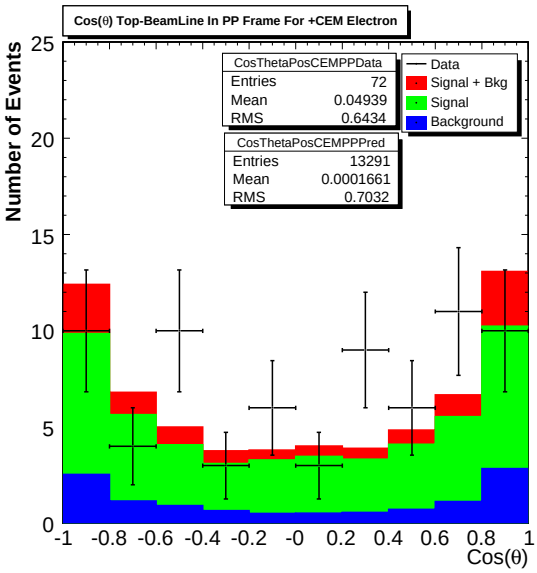

Figure 9.1: + Electron (CEM) $Cos(\Theta)$ Distribution

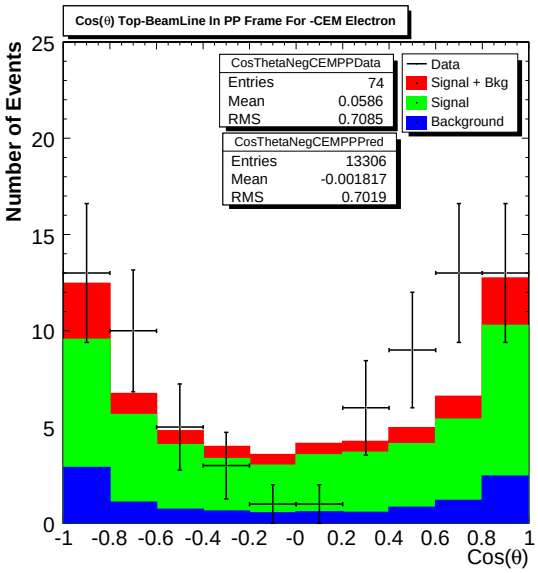

Figure 9.2: - Electron (CEM) $Cos(\Theta)$ Distribution

a CMUP muon:

$$A_{fb}^{+CMUP} = -0.38 \pm 0.16$$

$$A_{fb}^{-CMUP} = 0.14 \pm 0.17$$

$$A_{fb}^{CMUP} = -A_{fb}^{+CMUP} + A_{fb}^{-CMUP} = 0.25 \pm 0.12$$

We will return to this in section 9.5.

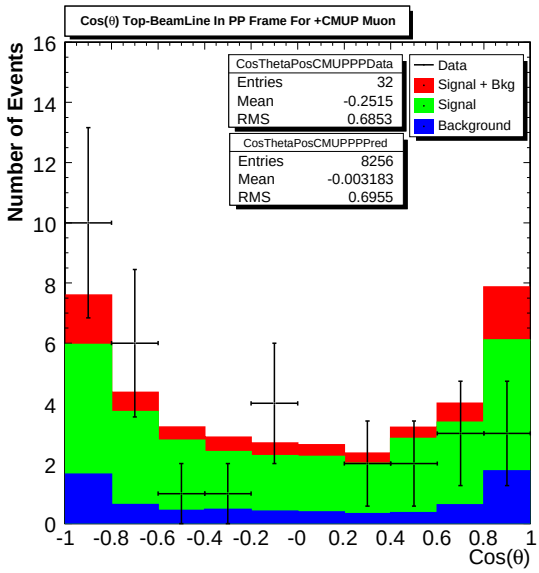

Figure 9.3: + Muon (CMUP) $Cos(\Theta)$ Distribution

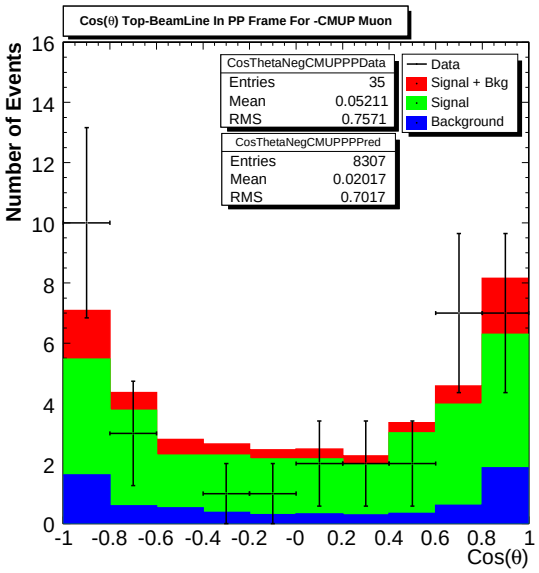

Figure 9.4: - Muon (CMUP) $Cos(\Theta)$ Distribution

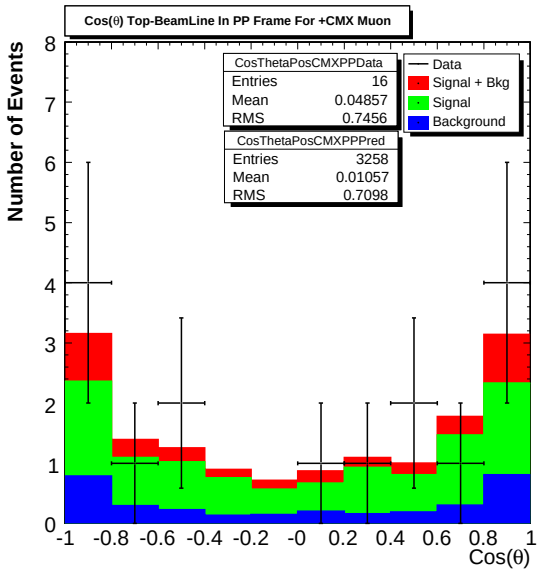

Figure 9.5: + Muon (CMX) $Cos(\Theta)$ Distribution

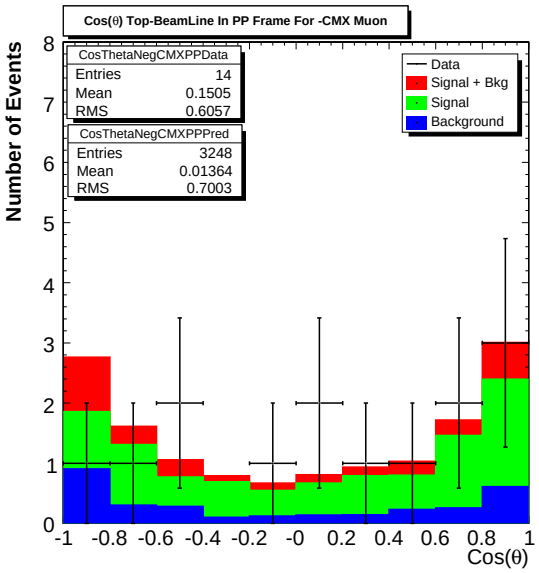

Figure 9.6: - Muon (CMX) $Cos(\Theta)$ Distribution

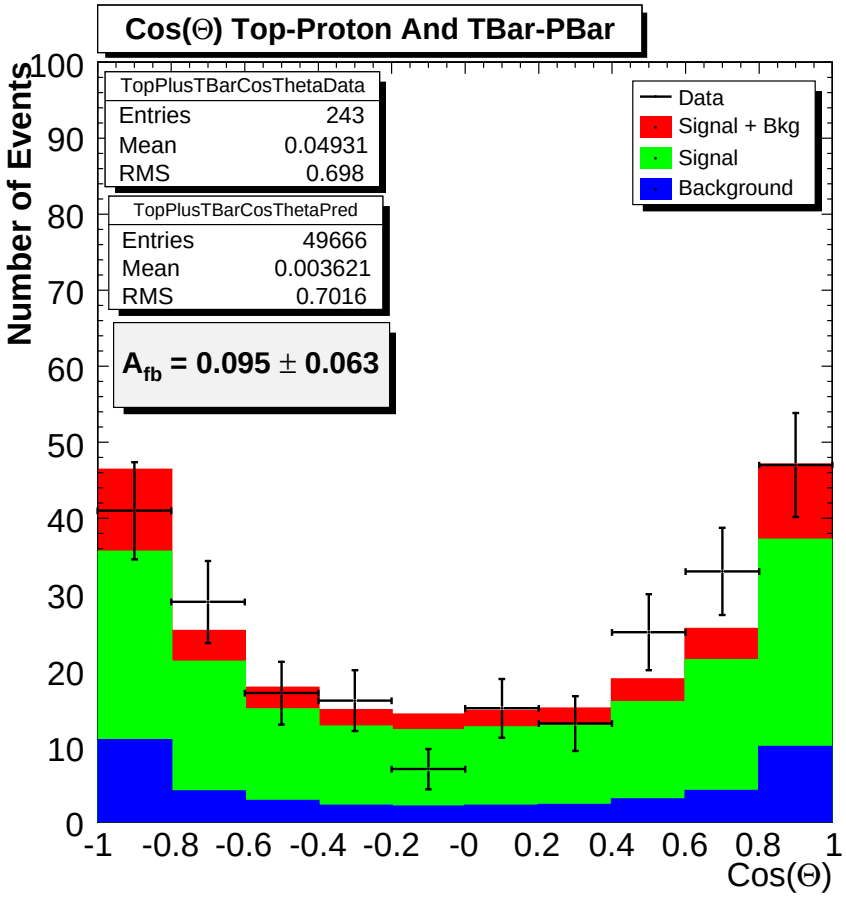

Figure 9.7: Combined Distribution

9.3 Correcting For Backgrounds

The predicted amount of background content in the forward/backward regions is subtracted from data for each of the six lepton categories. Table 9.4 shows the number of forward-backward events before and after subtraction and the background corrected asymmetry for each category. Because of the relatively small asymmetry in backgrounds, background processes for $t\bar{t}$ lepton plus jets events dilute, as opposed to bias, the measurement. The result is an increase in A_{fb} after correction in each category. The combined asymmetry after background subtraction is:

$$A_{fb}^{recon} = 0.126 \pm 0.078 \tag{9.4}$$

Table 9.4: Forward-Backward Asymmetry After Background Subtraction

Lepton Type	N_{Events}^{Recon} F-B	N_{Events}^{Bkg} F-B	$N_{Events}^{bkg-sub}$	$A_{fb}^{bkg-sub}$
+CEM	39-22	6.21-6.22	32.8-26.8	0.10±0.14
-CEM	42-32	6.04-6.30	36.0-25.7	0.17±0.14
+CMUP	10-22	3.72-3.86	6.28-18.1	-0.49±0.22
-CMUP	20-15	3.66-3.64	16.3-11.4	0.18±0.21
+CMX	9-7	1.79-1.71	7.2-5.3	0.15±0.32
-CMX	9-5	1.48-1.84	7.5-3.2	0.41±0.34

9.4 Correcting For Acceptance And Reconstruction

The correction procedure, equation 9.5 in chapter 7, is applied to the background corrected forward-backward values in Table 9.4 as shown below.

$$\begin{bmatrix} F_{corr} \\ B_{corr} \end{bmatrix} = M_{corr} \cdot \begin{bmatrix} F_{bkgsub} \\ B_{bkgsub} \end{bmatrix} \tag{9.5}$$

F_{bkgsub} and B_{bkgsub} are the number of background corrected forward and backward events, M^i_{corr} are the correction matrices for each lepton category i, and F_{corr} and B_{corr} are the final corrected forward and backward events. The resulting corrected forward backward asymmetries are shown in Table 9.5.

Because the detector and event selection are close to symmetric, the largest correction is for smearing effects in reconstruction. Smearing dilutes any underlying asymmetry that is present in the data and, therefore, applying the corrections increases the reconstructed asymmetry as is seen in Table 9.5 when compared to Table 9.4.

Table 9.5: Forward-Backward Asymmetry After Background Subtraction

Lepton Type	A_{fb}^{corr}
+CEM	0.13±0.19
-CEM	0.27±0.19
+CMUP	-0.69±0.30
-CMUP	0.28±0.29
+CMX	0.17±0.46
-CMX	0.58±0.46

The combined result, which is comparable to the predicted Standard Model value, 0.038, is:

$$A_{fb} = 0.20 \pm (0.11)^{stat} \pm (0.047)^{syst}$$

9.5 Discussion

Most of the non-zero value in the measured result is due to the large asymmetry in events with a CMUP muon events. If removed from the measurement, A_{fb} drops to 0.09±0.12. If the electron events are removed, A_{fb} increases to 0.39±0.18. Because CMX contributes only a small amount to our overall acceptance, CMX muon events have little effect on the measurement. If CMX is removed A_{fb} remains 0.20 ± 0.11.

All lepton categories have a positive asymmetry except events with a negative CMUP

muon. The asymmetry should have equal and opposite magnitudes for t and $\bar{t}$, assuming charge conjugation symmetry. Our statistical precision is unfortunately insufficient to see this expected result.

The measured asymmetry is consistent (at the 2σ level) with the theoretical prediction 0.038, and the shape of the combined production angle distribution in data is consistent with our model. The Tevatron should collect 8 fb^{-1} by the end of its life cycle. If the errors scale like $\sqrt{N}$, the statistical error on this measurement would be 0.04, comparable to the systematic error. If the measured asymmetry remains close to the current value, several other properties of the top quark can be measured in an attempt to identify the nature of the new physics. The mass of the top-antitop system can be used in conjunction with measurement of the asymmetry to search for a resonance corresponding with a peak in the asymmetry. This signature would provide evidence of a new production mechanism for top-antitop pairs in the form of a heavy neutral gauge boson. In the absence of such a resonance, a large asymmetry could point to new physics yet to be understood in the strong interaction.

Larger data sets at the LHC will be sensitive to an interesting charge asymmetry arising from pure QCD at NLO, expected to be of order 3.8%. The measurement procedure at the LHC will be complicated by the fact that the colliding particles there are proton-proton and therefore, the dominant production mechanism of $t\bar{t}$ pairs is gluon fusion, which has no asymmetry. Kuhn and Rodrigo have suggested an alternative measurement which will be sensitive to the QCD asymmetry, assuming several new obstacles can be overcome in the analysis [29].

CHAPTER 10

Conclusion

We have developed a method of reconstructing $t\bar{t}$ events in the lepton plus jets mode and applied this to a measurement of the front-back asymmetry in top production in 695 pb^{-1} of proton-antiproton collisions at $\sqrt{s} = 1.96$ TeV. The measurement is a test of charge asymmetry in the strong interaction at large momentum transfer. In the present data set it is also potentially sensitive to large parity violating contributions to top production. The front-back asymmetry is measured to be:

$$A_{fb} = 0.20 \pm (0.11)^{stat} \pm (0.047)^{syst}$$

The measured asymmetry is consistent (at the 2σ level) with the theoretical prediction 0.038, and the shape of the combined production angle distribution in data is consistent with our model. Most of the measured asymmetry is found to be coming from the muon sample. Our study of the front-back symmetry of the detector does not lead us to expect a systematic effect of this size in the muon system. Whether the effect is an unanticpated peculiarity of the CDF muon system or a statistical flunctuation or a real asymmetry can only be ascertained by study with a larger data set. The Tevatron should collect 8 fb^{-1} by the end of its life cycle. If the errors scale like $\sqrt{N}$, the statistical error on this measurement would be 0.04, comparable to the systematic error. If the measured asymmetry remains close to the current value, several other properties of the top quark

can be measured in an attempt to identify the nature of the new physics. The mass of the top-antitop system can be used in conjunction with measurement of the asymmetry to search for a resonance corresponding with a peak in the asymmetry. This signature would provide evidence of a new production mechanism for top-antitop pairs in the form of a heavy neutral gauge boson. In the absence of such a resonance, a large asymmetry could point to new physics yet to be understood in the strong interaction.

Larger data sets at the LHC will be sensitive to an interesting charge asymmetry arising from pure QCD at NLO, expected to be of order 3.8%. The measurement procedure at the LHC will be complicated by the fact that the colliding particles there are proton-proton and therefore, the dominant production mechanism of $t\bar{t}$ pairs is gluon fusion, which has no asymmetry. Kuhn and Rodrigo have suggested an alternative measurement which will be sensitive to the QCD asymmetry, assuming several new obstacles can be overcome in the analysis [29].

BIBLIOGRAPHY

[1] F.Abe et al., "Observation of the Top Quark in $p\bar{p}$ Collisions with the CDF Detector at Fermilab", Phys. Rev. Letters 74, 2626 (1995).

[2] M.Cacciari et al., JHEP 0404, 68 (2004)

[3] M.Beneke et al., "Top Quark Physics", CERN-TH-2000-100 (2000)

[4] A. Abulencia et al., CDF Collab., CDF conference note 7712 (2005).

[5] W. Pauli, "Niels Bohr and the Development of Physics", McGraw-Hill, NY (1955)

[6] J. H. Christenson, J. W. Cronin, V. L. Fitch, and R. Turlay, "Evidence for the 2π Decay of the K_2^0 Meson",Phys. Rev. Letters 13, 138 (1964).

[7] C.S Wu et al., "Experimental Test of Parity Conservation in Beta Decay", APS Phys Rev 105, 141301415 (1957).

[8] A. Angelopoulos et al. (CPLEAR collaboration),"First direct observation of time-reversal non-invariance in the neutral kaon system", Phys.Lett. B 444 (1998) 52.

[9] M.Carena, A.Daleo, B.A.Dobrescu, T.Tait, "Z' Gauge Bosons At The Tevatron", hep-ph/0408098 (2004).

[10] C.T. Hill, "Topcolor Assisted Technicolor", Phys. Lett. B 345, 483 (1995).

[11] S.Edielman et al., "Review of Particle Physics", Phys. Lett. B 592, 1 (2004).

[12] D. Acosta et al., "Measurement of the t anti-t production cross section in p anti-p collisions at $\sqrt{s} = 1.96$ TeV using lepton plus jets events with secondary vertex b-tagging", hep-ex/0411041.

[13] T. Affolder et al., Phys Rev D 64, 032002 (2001).

[14] A. Abulencia et al., CDF Collab., CDF conference note 8110 (2006), submitted to Phys. Rev. Lett.

[15] T. Sjostrand, S. Mrenna, and P. Skands. "Pythia 6.4: Physics and Manual", hep-ph/0603175 (2006).

[16] G. Corcella, I.G. Knowles, G. Marchesini, S. Moretti, K. Odagiri, P. Richardson, M.H. Seymour and B.R. Webber, "Herwig 6.5", JHEP 0101 (2001) 010, hep-ph/0011363 and hep-ph/0210213.

[17] S. Frixione and B.R. Webber, "Matching NLO QCD computations and parton shower simulations", JHEP 0206 (2002) 029 [hep-ph/0204244]
S. Frixione, P. Nason and B.R. Webber, "Matching NLO QCD and parton showers in heavy flavour production", JHEP 0308 (2003) 007 [hep-ph/0305252]

[18] F. Maltoni and T. Stelzer, JHEP 0302:027,2003
T. Stelzer and W.F. Long, Phys. Commun. 81 (1994) 357-371
H. Murayama, I. Watanabe, and K. Hagiwara, 1991

[19] M.L. Mangano, M. Moretti, F. Piccinini, R. Pittau, A. Polosa, "ALPGEN, a generator for hard multiparton processes in hadronic collisions", JHEP 0307:001,2003, hep-ph/0206293.

[20] D. Acosta et al., The CDF Collaboration, Phys. Rev. D71, 051104 (2005).

[21] F.James, "MINUIT: Function Minimization and Error Analysis Reference Manual", http://wwwasdoc.web.cern.ch/wwwasdoc/minuit/minmain.html, Computing And Networks Division, CERN (1998).

[22] CDF and D0 Collaborations, and the Tevatron Electroweak Working Group ,hep-ex/0603039 (2006).

[23] A. Abulencia et al., CDF Collab., CDF conference note 7794 (2005), submitted to Phys. Rev. Lett.

[24] D0 Collab., D0 conference note 4833 (2005).

[25] A. Abulencia et al., CDF Collab., CDF conference note 7804 (2005), Submitted to Phys. Rev. Lett.

[26] CDF Collaboration., CDF conference note 8087(2006).

[27] D. McGinnis et. al, "The Run II Handbook", Tech.Rep. http://www-ad.fnal.gov/runII", Fermilab Accelerator Devision, 2000.

[28] D. Amidei, "The CDF II Detector, Technical Design Report", Tech.Rep. FERMILAB-PUB-96-390-E, Fermi National Accelerator Laboratory, 1996.

[29] J.H. Kuhn and G. Rodrigo, Phys. Rev. Lett. 81, 49 (1998)
J.H. Kuhn and G. Rodrigo, Phys. Rev. D 59, 054017(1999).

[30] CDF Collaboration, CDF Conference Note 8125 (2006). http://www-cdf.fnal.gov/

[31] J.Pumplin et al., JHEP, 012 (2002)

[32] R.D.Field, See talks available at http://www.phys.ufl.edu/rfield/cdf/.

ABSTRACT

Measurement Of The Front Back Asymmetry In Top-Antitop Quark Pairs Produced In $p\bar{p}$ Collisions At $\sqrt{s} = 1.96$ TeV

by

Thomas A. Schwarz

Chair: Professor Dante E. Amidei

A method of reconstructing $t\bar{t}$ events in the lepton plus jets mode is applied to a measurement of the Top quark forward backward asymmetry using 243 $t\bar{t}$ pairs in 695 pb^{-1} of proton-antiproton collisions at $\sqrt{s} = 1.96$ TeV recorded at the Collider Detector Facility at Fermilab Tevatron. The measurement is a test of discrete symmetries in strong interactions. In the present data set it is potentially sensitive to large parity-violating contributions to top production such as a massive Z' boson. Larger data sets will have sensitivity for an interesting charge asymmetry arising from pure Quantum Chromodynamtics calculated at next-to-leading order.